Bioactive Materials 49 (2025) 342–361

Contents lists available at ScienceDirect

Bioactive Materials

journal homepage: www.keaipublishing.com/en/journals/bioactive-materials

Noninvasive method for achieving the regeneration of damaged nerves via ultrasonic nasal drops

Ning Zhu [a,b,1], Fan Wang [b,1], Zeyu Han [b,1], Shifeng Ling [b], Duo Wai-Chi Wong [c], Shenglin Ye [b], Mingyue Liu [b], Yanyang Chen [b], Gracie Shen [d], Ming Ni [b,*], Huitong Ruan [b,**], Yan Qiu [e,***], Wenguo Cui [b,****]

[a] School of Health Science and Engineering, University of Shanghai for Science and Technology, Shanghai, 200093, PR China
[b] Department of Orthopaedics, Shanghai Key Laboratory for Prevention and Treatment of Bone and Joint Diseases, Shanghai Institute of Traumatology and Orthopaedics, Ruijin Hospital, Shanghai Jiao Tong University School of Medicine, Shanghai, 200025, PR China
[c] Department of Biomedical Engineering, Faculty of Engineering, The Hong Kong Polytechnic University, Hong Kong, 999077, China
[d] Loomis Chaffee School, 4 Batchelder Road, Windsor, CT, 06095, USA
[e] Department of Pharmacy, Shanghai Pudong New Area People's Hospital, Shanghai, PR China

ARTICLE INFO

Keywords:
Hydrogel microspheres
Nasal-to-brain drug delivery
Ischemic stroke
Noninvasive regeneration
Piezoelectric materials

ABSTRACT

Repair and regeneration of damaged neurons is a promising therapeutic strategy for central nervous system (CNS) diseases such as ischemic stroke (IS). However, achieving efficient neuronal repair and regeneration after CNS injury through noninvasive methods remains a significant challenge. Therefore, this study proposes, for the first time, an ultrasonic nasal drop formulation that induces efficient regeneration of damaged neurons through electropharmacological coupling in an noninvasive manner. Liposomes containing the natural anti-inflammatory drug Timosaponin B-II (TB) were coated onto barium titanate nanoparticles (BTO) to form LTO@TB. Using microfluidic technology and a Schiff base reaction, LTO@TB was encapsulated into aldehyde-based and methacrylate-modified microspheres (MS) to create the ultrasonic nasal drop MS@LTO@TB. The aldehyde groups of MS@LTO@TB spontaneously formed amide bonds with the numerous amino groups in the nasal mucosa, facilitating specific adhesion. Due to its enhanced bioadhesion and efficient transmembrane transport, LTO@TB was continuously and noninvasively delivered to the brain when administered nasally. Additionally, under ultrasonic stimulation, LTO@TB in the brain exerted an electropharmacological coupling effect, achieving noninvasive electrical stimulation of damaged neurons. MS@LTO@TB modulated microglial phenotypes, restored electrical signal conduction among damaged neurons, reshaped the inflammatory microenvironment, reduced neuronal apoptosis, activated the PI3K/AKT signaling pathway, and promoted axonal regeneration. MS@LTO@TB also showed the unique ability to alleviate inflammation and promote neuronal remodeling in a mouse model of middle cerebral artery occlusion/reperfusion (MCAO/R). This study presents a promising strategy involving the nasal administration of ultrasonic nasal drops as a noninvasive and efficient treatment for CNS injuries.

1. Introduction

Neurological conditions affecting the central nervous system (CNS), such as ischemic stroke (IS), traumatic brain injury (TBI), and meningitis, are major global public health concerns [1–3]. After CNS injury, damaged neurons release damage-associated molecular patterns (DAMPs), leading to the activation of microglia into various functional states characterized by distinct molecular and phenotypic profiles.

Peer review under the responsibility of KeAi Communications Co., Ltd.
* Corresponding authors.
** Corresponding author.
*** Corresponding authors.
**** Corresponding author.
E-mail addresses: gendianqing@163.com (M. Ni), ruanhuitong@163.com (H. Ruan), Qiuyan@shpdph.com (Y. Qiu), wgcui80@hotmail.com (W. Cui).
[1] These authors contributed equally to this work.

https://doi.org/10.1016/j.bioactmat.2025.02.022
Received 8 October 2024; Received in revised form 23 January 2025; Accepted 13 February 2025

Proinflammatory microglia produce a diverse array of inflammatory mediators, including tumor necrosis factor-alpha (TNF-α) and interleukin-1 beta (IL-1β), which may exacerbate neuronal damage [4]. Concurrently, microglia can transition to activation states that support neuronal repair and regeneration. Therefore, modulating microglia from a proinflammatory to an anti-inflammatory phenotype to promote neuroprotective and reparative functions is essential for alleviating neuroinflammation and facilitating neuronal repair and regeneration. Clinically, pharmacological interventions have shown some efficacy in alleviating neuroinflammation [5,6]. The two main drug delivery routes for alleviating neuroinflammation are intravenous injection, which is invasive often results in low drug bioavailability due to the blood–brain barrier (BBB), and surgical delivery into the brain, which is also invasive and poses risks of mechanical cranial injury [7,8]. Thus, there is a pressing need to explore noninvasive and efficient drug delivery routes for treating CNS diseases (see Scheme 1).

Growing evidence indicates that the nasal-to-brain route is a promising pathway offers a viable non-invasive method for drug delivery to the brain [9]. This route bypasses the BBB via the trigeminal and olfactory nerves, allowing the delivery of medications directly to the brain. Moreover, when drugs are delivered via this route, loss of the drugs due to hepatic metabolism, renal filtration, gastrointestinal elimination, and serum degradation is avoided [10]. Therefore, nasal-to-brain drug delivery strategies hold significant clinical potential for the treatment of CNS injury. Considering the unique ability of the nasally administered drugs to bypass the BBB and be delivered efficiently to the CNS, Wu et al. investigated the effects of intranasal delivery of paeoniflorin nanocrystal formulations and found that it significantly increased the brain bioavailability of the nanocrystals [11]. Ruan et al. demonstrated the potential of delivering drugs via this route using a microneedle-mediated nasal-to-brain drug delivery system, which significantly improved drug delivery efficiency and therapeutic outcomes in Alzheimer's disease [12]. However, drug delivery strategies solely focused on inhibiting inflammatory cell infiltration often fail to achieve neuronal repair, leading to suboptimal treatment of CNS injury. Achieving efficient neuronal regeneration after CNS injury through noninvasive methods remains a challenge; thus, this study aims to address this challenge.

Taking IS as an example, the primary pathological mechanism is cerebral vascular occlusion, leading to interrupted cerebral blood flow. Currently, thrombolysis is the primary treatment with IS; however, reperfusion can trigger cerebral ischemia–reperfusion injury (CIRI), causing excessive local neuroinflammation and exacerbating neuronal damage [13]. Notably, IS-induced neuroinflammation disrupts nerve fiber integrity, interrupting electrical signal conduction between neurons, affecting neurotransmitter release and signaling, and ultimately causing neuronal degeneration and apoptosis. Therefore, to be effective, treatments for IS-induced CNS damage administered after thrombolysis need to both inhibit inflammatory cell infiltration and restore electrical signal conduction between damaged neurons. Standalone drug therapies can inhibit inflammatory cell infiltration but often fail to restore electrical signal conduction between damaged neurons, leading to suboptimal treatment of IS-induced CNS damage. The primary strategy to restore electrical signal conduction between damaged neurons involves electrode implantation to stimulate damaged neurons or bridge disrupted neural pathways, which is invasive [14]. Although effective, this approach carries risks of intracranial infection. Thus, identifying noninvasive methods to restore electrical signal conduction between damaged neurons is crucial. A novel noninvasive strategy to restore electrical signal conduction between damaged neurons uses piezoelectric materials. Piezoelectric materials, which act as electrical stimulators, are commonly used in neural tissue engineering. In a rat peripheral nerve injury model, US activated piezoelectric nanofiber-derived hydrogel conduits, generating localized electric charges via direct piezoelectric effect. This stimulation reinstated neuronal signal conduction and facilitated comprehensive nerve repair and regeneration, including enhanced axonal elongation and remyelination, thereby restoring functional neural connectivity [15]. The combination of nasal-to-brain delivery of anti-inflammatory drugs and noninvasive ultrasonic electrical stimulation could be a noninvasive approach to maximize therapeutic outcomes for IS patients.

This study proposes an ultrasonic nasal drop formulation for achieving efficient repair and regeneration of the damaged CNS after IS and thrombolysis in a noninvasive manner. In brief, liposomes containing the natural anti-inflammatory drug Timosaponin B-II (TB) were coated onto barium titanate nanoparticles (BTO) to form LTO@TB. LTO@TB was encapsulated into aldehyde-based and methacrylate-modified hyaluronic acid (HA) microspheres (MS) to create the ultrasonic nasal drop MS@LTO@TB. Notably, the aldehyde groups of MS@LTO@TB spontaneously formed Schiff bases with numerous amino groups in the olfactory region of the nasal mucosa. Due to the enhanced bioadhesion and efficient transmembrane transport of the ultrasonic drops, the delivery of the drug to the brain was significantly enhanced upon nasal administration. MS@LTO@TB modulated microglial phenotypes and restored electrical signal conduction between damaged neurons, reshaping the inflammatory microenvironment, reducing neuronal apoptosis, inducing the phosphorylation of proteins in the PI3K/AKT pathway, and promoting axonal regeneration.

In a murine model of middle cerebral artery occlusion/reperfusion (MCAO/R), MS@LTO@TB significantly decreased the infarct volume, alleviated CNS neuroinflammation, and enhanced cognitive function and memory. This system provides a completely noninvasive treatment for CNS injuries, effectively reducing secondary damage. Thus, the administration of ultrasonic nasal drops through the nasal-to-brain route represents a promising strategy for CNS treatment.

2. Materials and methods

2.1. Synthesis of Liposome@TB and LTO@TB

A mixture containing 60 mg of lecithin, 20 mg of cholesterol, 8.0 mg of stearyl amine, and 20 mg of TB was dissolved in 30 mL of chloroform. The chloroform was entirely evaporated at 35 °C for about 1 h, leaving behind a lipid film at the bottom of the round-bottom flask. Following this, 3 mL of double-distilled water mixed with PHB-dextran was added, and the flask was subjected to ultrasonication at 25 °C for 20 min to rehydrate the lipid film. This process resulted in the formation of micron-sized liposome bilayers. To obtain smaller liposome particles, the solution was probe sonicated for 5 min (60 pulses per minute, 130 W), yielding Liposome@TB. A 7:3 mass ratio blend of Liposome@TB and BTO was prepared and subsequently extruded through a 200-nm polycarbonate filter membrane with the aid of an Avanti Mini Extruder. The extrusion process was repeated 30 times to ensure efficient encapsulation of BTO within Liposome@TB, yielding the final product, LTO@TB.

2.2. Synthesis of AHAMA

To begin, 1 g of HA was mixed into 100 mL of deionized water until fully dissolved. Afterward, a 5 mL aliquot of 0.5 M sodium periodate solution was introduced dropwise to the solution. The resulting mixture was maintained under stirring in a dark environment at ambient temperature for 2 h. To neutralize any remaining sodium periodate, 1 mL of ethylene glycol was subsequently added, and the reaction continued for an additional hour. The product was then purified by dialysis for three days, followed by lyophilization, to yield aldehyde-functionalized hyaluronic acid (AHA). For methacrylation, the modified HA was further processed to obtain double bonds. Specifically, 1 g of HA was blended into 100 mL of water, followed by the addition of 1 ml of methacrylic anhydride (MA) to the mixture. The pH value was carefully controlled between 8 and 8.5 to facilitate the reaction, which proceeded over 12 h at a low temperature. Upon completion, the reaction product underwent dialysis for two days and was subsequently freeze-dried to obtain

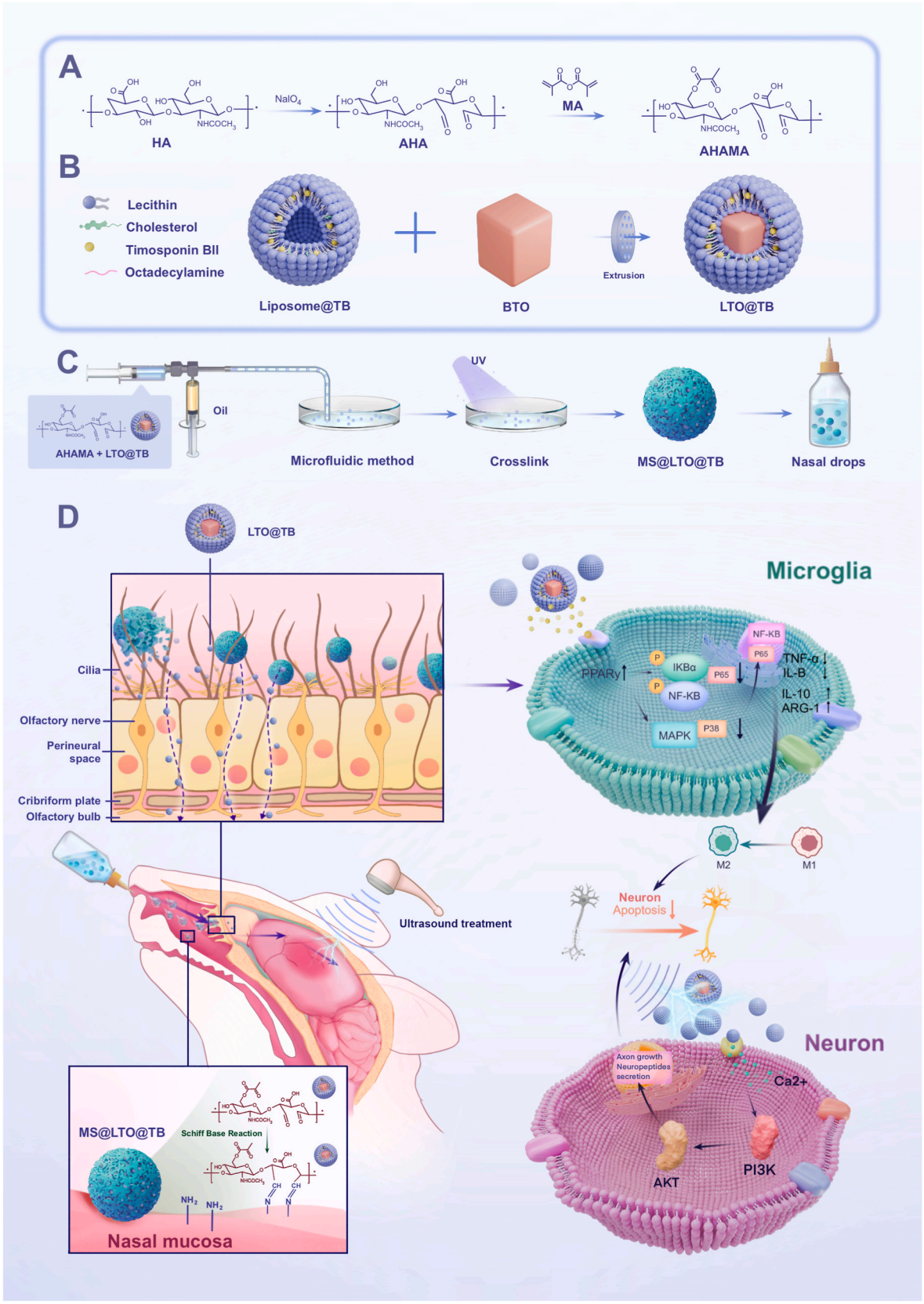

Scheme 1. Schematic diagram of how ultrasonic nasal drops noninvasively induce the regeneration of injured nerves. A) Synthesis of AHAMA hydrogels by sodium periodate oxidation and MA modification. HA and methacrylic anhydride (MA). B) Fabrication of LTO@TB via extrusion. C) Fabrication of MS@LTO@TB via microfluidic methods. D) Mechanisms by which MS@LTO@TB adheres to the nasal mucosa, pathways through which LTO@TB enters the brain ventricles, and mechanisms of microglial reprogramming by LTO@TB under US treatment, as well as the promotion of damaged nerve regeneration.

methacrylated aldehyde-functionalized hyaluronic acid (AHAMA).

2.3. Synthesis and characterization of MS and MS@LTO@TB

Hydrogel microspheres were prepared via microfluidic technology and photopolymerization. In brief, AHAMA, LTO@TB, and LAP (each at a 5 % mass ratio) were used as the dispersed phase, and liquid paraffin with 5 % Span 80 served as the continuous phase. A droplet microfluidic device sheared the dispersed phase into droplets via the continuous phase. The droplets were collected at −20 °C, frozen overnight at −80 °C, and then photopolymerized via 405 nm UV light for 15 min. The microspheres were collected, rinsed with diethyl ether and PBS, and freeze-dried for further experiments. The morphology and size of the MS@LTO@TB were examined with a bright-field microscope (ZEISS, Germany). The microspheres' morphology was further examined via laser confocal microscopy. MS and MS@LTO@TB were coated with gold for 120 s with an ion sputter coater, and then their surface morphology and microstructure were analyzed via SEM. An accelerating voltage of 15 kV captured the images.

2.4. Characterization of MS@LTO@TB

XPS was conducted on the ESCALAB 250Xi system (Thermo Fisher Scientific, USA) using a monochromatic Al Kα radiation source with an energy of 1486.6 eV in high-resolution mode. Raman spectroscopy was carried out with the LabRAM HR Evolution spectrometer (HORIBA JY, France) under 532 nm laser excitation. Measurements of hydrodynamic diameter and zeta potential were performed using dynamic light scattering (DLS) on the DelsaMax Pro instrument (Beckman Coulter, USA). Piezoelectric force microscopy (PFM) was utilized to capture images and amplitude butterfly loops of BTO using an MFP-3D atomic force microscope (Asylum Research) in contact mode with a conductive probe operating in PFM mode. The polarization-electric field hysteresis loops were recorded using an RTI-MultiFerroic ferroelectric testing system (Radiant, USA).

2.5. Characterization of the piezoelectric properties of MS@LTO@TB

To evaluate the piezoelectric performance of MS@LTO@TB, a flexible gold electrode was positioned at the base of a mold. MS@LTO@TB material was carefully introduced into the mold, followed by placing another gold electrode on top. The piezoelectric response was measured using a digital multimeter (Keithley 6514, USA) connected to a testing system and a computer-controlled programmable linear motor. Periodic compression of the generator was applied by the linear motor, and the corresponding voltage outputs under varying pressures or ultrasonic stimulation were recorded via the multimeter.

2.6. In vitro degradation test

The biodegradability of MS and MS@LTO@TB was assessed through enzymatic degradation experiments. Degradation kinetics experiments were performed at room temperature. In brief, 10 mg of MS or MS@LTO@TB was immersed in 1000 U/mL hyaluronidase solution and incubated at 37 °C in a shaker, and degradation was assessed. The hyaluronidase solution was replaced with fresh 1000 U/mL enzyme solution every three days. Samples were collected every seven days, and excess PBS was removed with filter paper. Each sample was weighed, and its weight at different time points was compared to its initial weight. Changes in the morphology of the microspheres were observed and analyzed.

2.7. Encapsulation efficiency assay

A 1 mg sample of MS@LTO@TB was fully disintegrated, and the optical density (OD) value was measured with a UV-5100 spectrophotometer (Metash, China). The encapsulation efficiency was calculated as follows:

$$\text{Encapsulation efficiency } (\%) = \frac{\text{Weight of encapsulated TB}}{\text{Initial weight of TB added}} \times 100\%.$$

2.8. Drug release assay

Under 37 °C conditions, the MS@LTO@TB samples were soaked in 1 mL of ddH2O buffer containing hyaluronidase (1000 U/mL) and gently stirred at 100 rpm. Release medium samples were collected at predetermined time intervals for liquid chromatography-mass spectrometry (LC-MS) analysis, after which the release medium was replaced with 1 mL of fresh ddH2O solution containing hyaluronidase (1000 U/mL). After all samples were collected, LC-MS detection was performed using a Waters XTerra™ MS C18 column, with a mobile phase consisting of methanol, acetonitrile, and 10 mmol L^{-1} ammonium acetate at a ratio of 37.5:37.5:25. The flow rate was set to 0.2 mL min^{-1}, and the extraction mobile phase was a mixture of acetonitrile and 10 mmol L^{-1} ammonium acetate solution. The mass spectrometry analysis was conducted using an electrospray ionization (ESI) source in negative ion mode, employing selected reaction monitoring (SRM) to monitor the ion transition from *m/z* 919.4→*m/z* 757.4, with a scan time of 100 ms. The ion spray voltage was set at 4.5 kV, the capillary voltage at 44 V, and the source temperature at 270 °C. The sheath gas flow rate was 10 arb, the auxiliary gas flow rate was 12 arb, and the sweep gas flow rate was 5 arb. The TB protonated molecular ion peak $[M-H]^-$ at *m/z* 919 was obtained in the full-scan mass spectrum, and the major fragment ion at *m/z* 757 generated by the fragmentation of the protonated molecular ion was used for quantitative analysis. The concentration of TB in the solution over time was plotted as a release curve to evaluate the drug release behavior.

2.9. Measurement of the mucosal adhesion of MS@LTO@TB

In this experiment, the toad's palatal ciliary movement model was used to evaluate the nasal mucosal adhesion of MS@LTO@TB and HAMA@LTO@TB. First, the toad's spinal cord was disrupted with a probe, rendering it temporarily immobile to ensure it remained still during the experiment. The toad was then placed on a dissection board and secured in a supine position using fixation pins to ensure complete exposure of the palatal mucosa. To prevent interference, hemostatic forceps were applied to keep the toad's mouth open, ensuring that the palatal mucosa was clearly visible. Subsequently, MS@LTO@TB or HAMA@LTO@TB was evenly applied to the exposed palatal mucosal surface using a microliter syringe, with the application area located between the anterior margin of the eye socket and the oral cavity, ensuring that the critical region of the mucosa was covered. After administration, the cilia on the mucosa naturally began to move the drug particles toward the esophageal opening. To quantitatively assess the drug's adhesion and the ciliary clearance rate, the time taken for the drug particles to travel from the application point to the esophageal opening (approximately 1 cm) was recorded to evaluate the mucosal retention time of the drug. Each toad underwent six independent measurements to ensure the reliability and consistency of the data. After each measurement, the hemostatic forceps were released, allowing the toad's mouth to close naturally, followed by a 10-min rest period to allow the mucosal surface to rehydrate and prevent drying from affecting ciliary movement. Finally, by recording the data from each experiment, the mucosal retention time and nasal ciliary clearance rate of MS@LTO@TB and HAMA@LTO@TB were calculated, systematically assessing their adhesion to the nasal mucosa.

2.10. Cell culture

BV-2 cells, generously provided by Procell Life Science & Technology

Co., Ltd., were cultured in Dulbecco's Modified Eagle's Medium (DMEM; Gibco) supplemented with 10 % fetal bovine serum (FBS) and 1 % penicillin-streptomycin solution (Gibco). The cells were incubated at 37 °C in a humidified environment with 5 % CO_2. The culture medium was refreshed daily, and the cells were subcultured every two days. PC-12 cells, obtained from Procell Life Science & Technology Co., Ltd. (CL-0481), were grown in PC-12 cell-specific medium (CM-0481, Procell) under the same conditions as BV-2 cells.

2.11. Coculture of MS@LTO@TB with BV-2 cells

BV-2 cells (1×10^5 cells per well) were plated into 24-well plates and allowed to grow for 24 h. Following this, the cells were exposed to 100 ng/mL of LPS for 24 h to activate the inflammatory response. The activated BV-2 cells were then cocultured with MS@LTO, cocultured with MS@LTO@TB, or cocultured with MS@LTO@TB and subjected to US treatment. The cells were subsequently stained with an anti-F4/80 antibody (Beyotime, China), an anti-F-actin antibody (Beyotime, China), and DAPI, followed by examination via LSCM.

2.12. Construction of a transwell model

The cells were then stimulated with 100 ng/mL LPS for 24 h to induce inflammatory activation. The activated BV2 cells were cocultured with MS@LTO, cocultured with MS@LTO@TB, or cocultured with MS@LTO@TB and subjected to US treatment. The cells were then stained with an anti-F4/80 antibody (Beyotime, China), an anti-F-actin antibody (Beyotime, China), and DAPI and examined via LSCM.

2.13. In vitro cytotoxicity evaluation

Cytotoxicity was assessed via the Cell Counting Kit-8 (CCK-8) assay. PC-12 and BV-2 cells were cultured in 96-well plates at a density of 10^4 cells per well. The cells were incubated with 200 μL of medium containing 10 % fetal bovine serum (FBS, Gibco) for 12 h. The cells were subsequently incubated for an additional 24 h. After 24 h, 10 μL of CCK-8 reagent was added to each well, and the plates were incubated for 1 h. The absorbance was measured at 450 nm with a microplate reader (Molecular Devices, FlexStation3). The formula for calculating cell viability is as follows:

$$\text{Cell viability} = \frac{ODsample - ODblank}{ODcontrol - ODblank} \times 100\ (\%).$$

2.14. Flow cytometry

To measure PC-12 cell apoptosis, both floating and adherent cells were harvested and stained using an Annexin V-FITC apoptosis detection kit (Beyotime, China). To identify the activation state of BV-2 cells, BV-2 cells were incubated with antibodies against the proinflammatory marker (CD86) and anti-inflammatory marker (CD206) for 30 min. After being washed three times with PBS, the cells were analyzed with a flow cytometer (BD, LSRFortessa X-20, USA). The data were analyzed with FlowJo v10.0 software. The antibodies used included anti-CD86 (1:2000, Thermo Fisher Scientific) and anti-CD206 (1:2000, Thermo Fisher Scientific) antibodies.

2.15. Immunofluorescence

After fixation and blocking, the samples were incubated with the primary antibody overnight at 4 °C. Subsequently, they were exposed to goat anti-rabbit IgG H&L (Alexa Fluor 488, Beyotime, China) or goat anti-mouse IgG H&L (Alexa Fluor 488, Beyotime, China) for 1 h at room temperature. Finally, the nucleus and cytoskeleton were stained with Actin-Tracker Red555 (Beyotime, China), an anti-F4/80 antibody (Beyotime, China), an anti-β-tubulin antibody (Beyotime, China), and DAPI (Beyotime, China). Each staining step involved at least three washes with PBS.

2.16. Measurement of the intracellular Ca^{2+} concentration

To assess intracellular Ca^{2+} levels in treated PC-12 cells, 200 μL of Fluo-4 AM solution (Beyotime, China) was added, and the cells were incubated at 37 °C under dark conditions for 30 min. Afterward, PBS was used to wash the cells gently. The cells were then observed using a fluorescence microscope, and ImageJ software was applied to quantify the relative fluorescence intensity of intracellular calcium.

2.17. Western blotting

Total protein was extracted, and its concentration was quantified before separating the proteins via electrophoresis and transferring them onto a PVDF membrane. The membrane was first blocked with Quick-Block™ Blocking Buffer (Beyotime, China) for 30 min, followed by overnight incubation at 4 °C with primary antibodies. After being washed three times with Western Wash Buffer (Beyotime, China), the membrane was incubated with a secondary antibody—either goat anti-mouse (1:400, Beyotime, China) or goat anti-rabbit (1:400, Beyotime, China)—for 1.5 h at room temperature. Protein bands were visualized using a chemiluminescence detection system (ChemiDoc™ Touch Imaging System, Bio-Rad).

The primary antibodies used in this assay included anti-PPARγ (1:1000, Abcam), anti-NF-κB p65 (1:1000, Abcam), anti-phospho-NF-κB p65 (1:1000, Abcam), anti-p38 MAPK (1:1000, Abcam), anti-PI3K (1:1000, Abcam), anti-AKT (1:1000, Abcam), anti-phospho-PI3K (1:1000, Abcam), anti-phospho-AKT (1:1000, Abcam) and anti-βactin (1:1000, Abcam).

2.18. Experimental animals

All the animal experiments were approved by the Animal Research Committee of Shanghai Pudong New Area People's Hospital (Ethical Approval No. 2022K83). Male C57 BL/6J mice, weighing 22 ± 2 g, were obtained from Shanghai Vitron Lever Laboratory Animal Technology Co., Ltd. The rats were housed in a specific pathogen-free (SPF) animal facility under controlled conditions at a temperature of 26 ± 2 °C and humidity of 55 ± 10 % on a 12-h light–dark cycle. The rats were given ad libitum access to food and water.

2.19. In vivo intranasal administration

This study administered intranasal doses using a PBS suspension formulation, utilizing a microliter syringe to ensure consistency and accuracy of administration. After securing the mice in a supine position, 20 μL of the MS@LTO@TB PBS suspension was administered to each nostril of every mouse using a microliter syringe, totaling 40 μL (resulting in a TB intake of 40 mg/kg per mouse). The administration process was performed under mild isoflurane anesthesia to reduce the mice's stress response and ensure the accurate deposition of the drug onto the nasal mucosa. Immediately after administration, the noses were pinched to prevent the drug from leaking out.

2.20. In vivo fluorescence imaging

After C57BL/6J mice received intranasal administration of MS@LTO, intranasal administration of MS@LTO@TB, or intranasal administration of MS@LTO@TB combined with ultrasound (US) treatment, the fluorescence intensity was measured on days 1, 3, 5, 7, and 14 via an IVIS Spectrum system (Xenogen, USA).

2.21. Preparation of the MCAO/R model

To induce anesthesia, the mice received an intraperitoneal injection of sodium pentobarbital (40 mg/kg). The mice were placed in the supine position on an operating table, with the incisors and limbs secured to stretch the neck skin flat. The neck fur was shaved, cleaned, and disinfected. The subcutaneous tissue was bluntly dissected to expose the pretracheal muscles. Dissection continued along the right sternocleidomastoid muscle tendon downward until the carotid sheath was visualized. The carotid sheath was gently retracted upward to expose the right common carotid artery (CCA). The CCA, external carotid artery (ECA), and internal carotid artery (ICA) were carefully dissected for exposure. Nonabsorbable 10–0 sutures were used to ligate the ECA and the proximal portion of the CCA. A microvascular clip was used to clamp the ICA. A suture was placed under the bifurcation of the CCA, and a knot was tied. A minor incision was performed in the CCA between the knot and the ligation point with ophthalmic scissors. A guide wire was inserted and advanced approximately 1 cm into the ICA until slight resistance was felt, indicating proper placement, and then the suture was tightened. The incision was sutured, and the skin was disinfected with an alcohol swab. The suture end was secured to the skin, and after 1 h of ischemia, it was carefully removed to initiate reperfusion. Sterile saline was administered intraperitoneally to prevent dehydration postsurgery. Sham surgery was performed on the control group following the same procedure without insertion of the suture.

2.22. Measurement of brain edema

Within 24 h of the final treatment, the mice were anesthetized and swiftly decapitated to extract their brains. The olfactory bulbs, cerebellum, and lower brainstem were carefully removed, followed by the separation of the left and right cerebral hemispheres. Brain tissues were immediately placed on moist filter paper, and their wet weight was measured using an electronic balance. The weights were recorded, and the tissues were then dried in an oven at 105 °C for 24 h. Once dried, the dry weight was measured, and the brain water content for each group was calculated using the following formula:

$$\text{Brain water content } (\%) = \frac{\text{wet weight} - \text{dry weight}le}{\text{wet weight}} \times 100\%.$$

2.23. TTC staining for assessment of cerebral infarct volume

After administering sodium pentobarbital via intraperitoneal injection to induce anesthesia, the mice were decapitated for the immediate retrieval of brain tissue. The brain tissue was fixed at −20 °C for 1 h. Using a fine blade, the brain tissue was placed in a specialized mold and sectioned perpendicular to the longitudinal axis into six slices, each approximately 2 mm thick. The slices were immersed in 2 % TTC solution (Servicebio, China) and incubated at 37 °C in the dark for 15 min. After the incubation period, the brain sections were thoroughly washed with PBS and subsequently immersed in 4 % paraformaldehyde (Sigma-Aldrich, USA) for 24 h for fixation. The stained slices were arranged in sequential order. The red areas represented normal tissue, whereas the white areas represented infarcted tissue. The infarct area and volume were calculated with ImageJ software as follows:

$$\text{Infarct volume} = \text{sum of infarct areas in all slices} \times \text{slice thickness};$$

$$\text{Infarct volume percentage } (\%) = \frac{\text{infarct volume}}{\text{total brain volume}} \times 100\%.$$

2.24. Measurement of cytokine levels in the brain

The brain tissues were homogenized in saline solution and then centrifuged at 12,000 rpm for 5 min. The levels of IL-6, TNF-α, Arg-1, and IL-10 in the resulting supernatant were measured using ELISA kits, including IL-6 and TNF-α kits (Proteintech, Wuhan, China), an Arg-1 kit (Cloud-Clone, Wuhan, China), and an IL-10 kit (Proteintech, Wuhan, China), according to the manufacturers' protocols.

2.25. Open field testing

Mice were placed in the middle of a square open field arena (40 cm × 40 cm × 40 cm), with the arena divided into two sections: a central region and an outer peripheral area. The central section was delineated as a square area 10 cm inward from the surrounding walls, with the rest of the space categorized as the peripheral section. The mice were allowed to explore the arena freely for 10 min while their movements were recorded using a video camera. The recorded data were processed with Smart v3.0 software to calculate the total distance traveled (cm), average speed (cm/s), and time spent in the central area (s) during the 10-min session. After each trial, the arena was cleaned with 30 % ethanol to eliminate odors and reduce data variability.

2.26. Barnes maze test

Each mouse was initially placed in the center of the maze platform under a cylindrical start box for a 30-s acclimation period. After removing the start box, the mouse was allowed to explore freely for 3 min. If the mouse did not find the target hole during this time, it was carefully guided to the hole and kept in the dark escape box for 1 min to aid adaptation. If the target hole was found within 3 min, the mouse was allowed to remain in the escape box for 1 min to consolidate spatial memory before returning to its home cage. To avoid odor contamination and reduce variability, the maze and escape box were sanitized with 30 % ethanol after each session. Training consisted of two daily sessions with at least 15 min between trials, repeated over three consecutive days. The maze platform was rotated each day to eliminate reliance on nonspatial cues, such as physical inclines, for locating the target hole. The latency for each mouse to locate and enter the target hole was recorded and analyzed automatically using Smart v3.0 software.

2.27. In vivo biosafety evaluation

Blood was drawn within 24 h after the final treatment for routine hematology tests. The brain, heart, liver, spleen, lungs, and kidneys were harvested and subjected to histological evaluation through hematoxylin and eosin (H&E) staining, along with Nissl staining.

2.28. Immunohistochemical analysis

Tissue sections were incubated with primary antibodies at 4 °C for 12 h, followed by incubation with enzyme-conjugated secondary antibodies at room temperature for 2 h. Finally, DAB staining was performed. Each staining step was followed by at least three washes with PBS. The samples were then observed, and images were captured via a bright-field microscope. The following primary antibodies were used: anti-CD206 (1:50, ABclonal), anti-CD86 (1:50, ABclonal), anti-MAP2 (1:50, ABclonal), and anti-Tuj1 (1:200, ABclonal) antibodies.

2.29. Transcriptome sequencing and data analysis

At 14 days post-surgery, the experimental mice were euthanized, and fresh brain tissues were collected. Subsequently, the samples were divided into three groups: Control, MCAO/R, and MS@LTO@TB, each consisting of three biological replicates. The fresh brain tissue samples were promptly frozen in liquid nitrogen, and total RNA was extracted using Trizol reagent. RNA libraries were constructed using the NEBNext Ultra II RNA Library Prep Kit (#E7490). High-throughput sequencing was performed by Shanghai Shenggong Biotechnology Co., Ltd. on the Illumina NovaSeq 6000 platform, employing a 150 bp paired-end sequencing strategy. The raw sequencing data were first quality

assessed using FastQC (v0.11.9) and then processed with Trimmomatic (v0.39) to remove low-quality reads and adapter sequences. Gene expression quantification was conducted using FeatureCounts (v2.0.1) to generate a count matrix of gene expression. After obtaining the count matrix, data normalization and differential expression analysis were performed using the DESeq2 package (v1.30.1) with a threshold of p-value <0.05 and $|\log_2\text{FoldChange}| > 1$. Finally, GO and KEGG enrichment analyses of the differentially expressed genes were carried out using the ClusterProfiler package (v4.0.5). RNA sequencing and preliminary data processing were completed by Shanghai Shenggong Biotechnology Co., Ltd.

2.30. Statistical analysis

All experiments were performed in triplicate or more ($n \geq 3$). Statistical analysis and graph preparation were conducted using GraphPad Prism 8.0 (GraphPad Software Inc., USA). Quantitative data with a normal distribution and homogeneity of variance are presented as mean ± standard deviation (mean ± SD). Differences between two groups were assessed using an independent samples *t*-test, while comparisons among multiple groups were evaluated with one-way or two-way ANOVA followed by Tukey's post hoc test. A p-value <0.05 was considered to indicate statistical significance.

3. Results and discussion

3.1. Synthesis and characterization of LTO@TB

LTO@TB was synthesized via the lipid extrusion method. Transmission electron microscopy (TEM) revealed that BTO had a typical tetragonal structure, with a diameter of approximately 50 nm (Fig. S1). Liposomes, as drug carriers, are ideal for transporting various drugs. Their unique features include an internal aqueous core, which is ideal for transporting hydrophilic drugs, and a bilayer structure, which is ideal for transporting for hydrophobic drugs [16]. Using the thin-film dispersion technique, Liposome@TB was prepared by incorporating lecithin, cholesterol, stearyl amine, and TB. LTO@TB was formed by mixing Liposome@TB and BTO at a mass ratio of 7:3 and multiple extrusions via a liposome extruder. Thus, this ratio was chosen for subsequent experiments. Scanning electron microscopy (SEM) revealed that the LTO@TB are uniformly distributed, with sizes ranging from 50 to 100 nm (Fig. 1A). TEM analysis confirmed the fabrication of LTO@TB, with the outer light-colored membrane identified as Liposome@TB and the inner dark region identified as BTO (Fig. 1B). High-resolution TEM (HRTEM) revealed that LTO@TB had a single-crystal structure with a lattice spacing of 0.25 nm, likely corresponding to the (110) crystal plane (Fig. 1C). The selected area electron diffraction (SAED) patterns

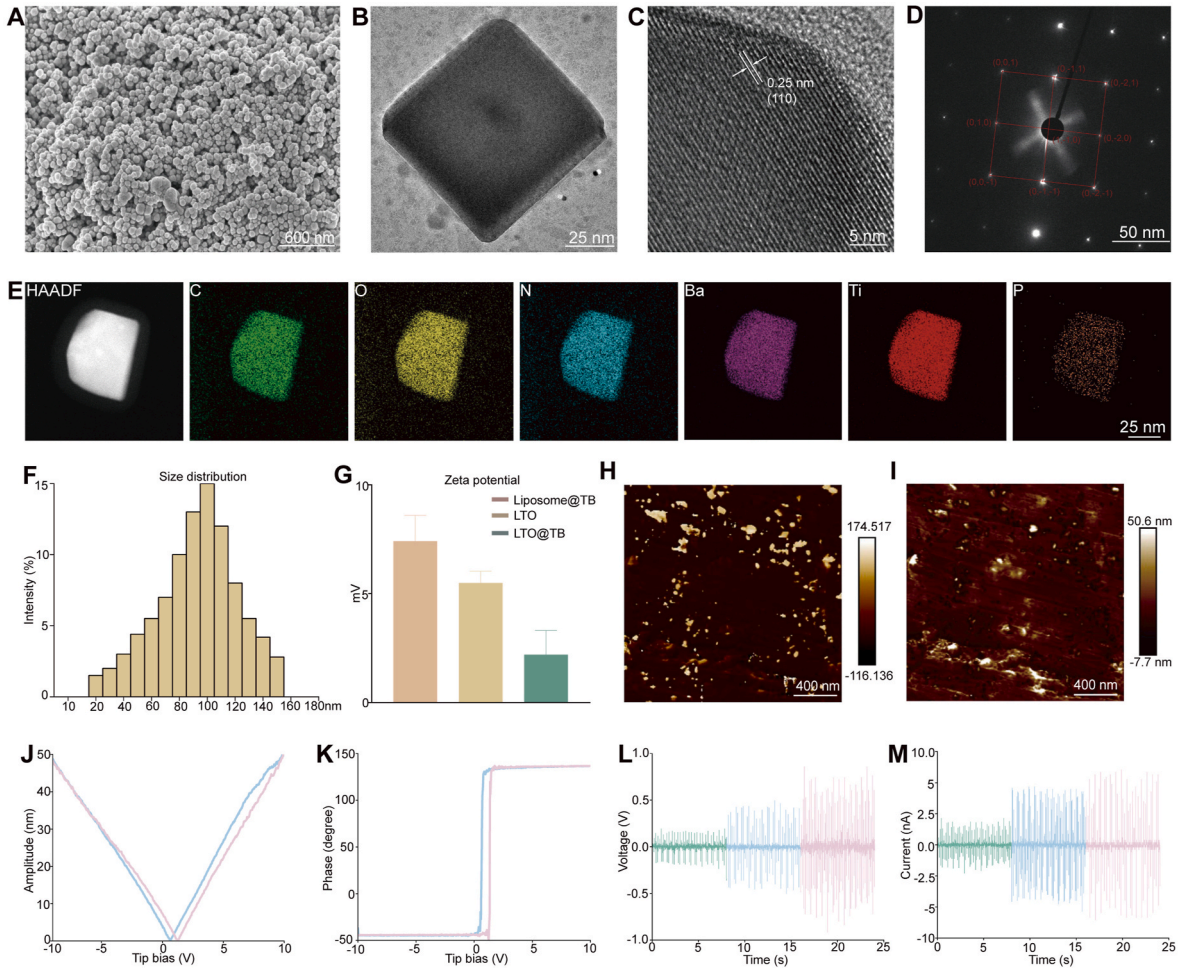

Fig. 1. Structural characterization and piezoelectric properties of LTO@TB. A) SEM image of LTO@TB. Scale bar, 600 nm. B) TEM image of LTO@TB. Scale bar, 25 nm. C) HRTEM image of LTO@TB. Scale bar, 5 nm. D) SAED pattern of LTO@TB. E) HAADF elemental mapping of LTO@TB. Scale bar, 25 nm. F) Size distribution of LTO@TB. G) Zeta potentials of Liposome@TB, LTO and LTO@TB. H) Height of LTO@TB. Scale bar, 400 nm. I) Piezoelectric amplitude of LTO@TB. Scale bar, 400 nm. J, K) Amplitude loop curve and phase loop curve of LTO@TB at an AC voltage from −10 V to 10 V. L) Open-circuit voltage of the device made from LTO@TB under US stimulation within the frequency range of 0.5–1.5 W. M) Open-circuit current of the device made from LTO@TB under US stimulation within the frequency range of 0.5–1.5 W. The data are presented as mean ± standard deviation (SD) ($n = 3$) for each group.

revealed characteristic crystallographic orientations of LTO@TB, with diffraction spots indexed to specific planes: (0, 0, 1), (0, −1, 1), (0, −2, 1), (0, −2, 0), (0, −2, −1), (0, −1, −1), (0, 0, −1), and (0, 1, 0) (Fig. 1D). High-angle annular dark-field (HADDF) imaging further confirmed the elemental distribution within LTO@TB (Fig. 1E). Further investigation revealed that mixing of Liposome@TB and BTO at a mass ratio of 7:3 resulted in encapsulation efficiencies of approximately 77 % ± 3 % for Liposome@TB and 50 % ± 4 % for LTO@TB, with drug loading rates of approximately 16 % and 11 %, respectively (Figs. S3 and 4). Particle size is a crucial factor in nanodrug nasal delivery systems. Smaller nanoparticles experience reduced resistance during nasal transport, which facilitates the delivery of the drug to the brain via transcellular or paracellular pathways, thus enhancing the transfer to the ventricles of the brain [17]. Research indicates that a particle size of around 100 nm is optimal for nanodrug delivery through olfactory pathways, a constraint mainly dictated by the diameter of the olfactory nerve axons [18]. Furthermore, the lecithin content can be adjusted to control the liposome diameter. In this study, the average diameters of LTO@TB and Liposome@TB nanoparticles were 101 ± 14.5 nm and 108 ± 15.7 nm, respectively (Fig. 1F, Fig. S5), which meet the ideal size requirements for nanodrug delivery via olfactory axons. In addition to particle size, the surface charge of the carrier significantly influences the interaction of nanodrugs with the nasal mucosa and their diffusion along olfactory nerve axons. Given that the nasal mucosa is typically negatively charged, positively charged nanodrug delivery systems are more likely to interact with it via electrostatic attraction, thereby prolonging the time the drug remains in the nasal cavity and enhancing its absorption [19]. A study on lipid carriers for nasal administration showed that positively charged nanostructured lipid carriers exhibited significantly higher plasma bioavailability compared to their negatively charged counterparts [19]. The incorporation of stearyl amine into liposomes, Liposome@TB, and LTO@TB resulted in positive zeta potentials, i.e., 7.5 ± 1.3 mV, 5.3 ± 0.6 mV, and 2.3 ± 0.9 mV, respectively (Fig. 1G); thus, stearyl amine facilitated the interaction of LTO@TB with the nasal mucosa, prolonged the amount of time that LTO@TB remained in the nasal cavity, and increased its absorption.

To investigate the piezoelectric properties of LTO@TB, piezoelectric force microscopy (PFM) of LTO@TB thermally deposited on a conductive silicon substrate was performed. In the amplitude and phase images obtained under an applied voltage bias, the bright and dark regions were strongly correlated, confirming the piezoelectricity of LTO@TB (Fig. 1H and I). A characteristic butterfly amplitude was observed upon application of a 10 V AC voltage (Fig. 1J). The phase diagram showed a distinct 180° hysteresis loop in LTO@TB, demonstrating its strong piezoelectric response and confirming the presence of ferroelectric domains (Fig. 1K). Additionally, the d33 curve indicated that the piezoelectric constant of LTO@TB was approximately 13.75 p.m./V. LTO@TB showed significant open-circuit voltage and current responses under different US intensities (0.5 W, 1 W, and 1.5 W). At an US intensity of 0.5 W, the open-circuit voltage ranged from −0.3 V to 0.3 V, and the current intensity ranged from −2 nA to 2 nA (green). When the US intensity increased to 1 W and 1.5 W, the maximum voltage rose to 0.5 V and 0.7 V, with the maximum current intensity reaching 4 nA and 6 nA (blue, pink) (Fig. 1L and M). The intensity of the voltage and current response of LTO@TB were positively correlated with the applied US intensity, indicating sensitivity to ultrasonic stimulation.

3.2. Synthesis and characterization of MS@LTO@TB

The nasal cavity is anatomically divided into three distinct functional regions: the nasal vestibule, the respiratory region, and the olfactory region [20]. Among these, the olfactory region is of paramount importance, serving as the primary pathway for delivering drugs to the brain through the nasal route. The nasal mucosa, which forms the lining of the nasal cavity, consists of epithelial tissue and the underlying lamina propria. In the olfactory region, the mucosal layer is predominantly composed of supporting cells (SCs), whose amino-rich cell membranes play an essential role in maintaining both the structural integrity and physiological stability of the olfactory mucosa [21]. By exploiting the distinctive physiological environment of the olfactory mucosa, we utilized microfluidic and photocrosslinking technologies to dynamically load LTO@TB into microspheres (MS). Aldehyde-based and methacrylate-modified hyaluronic acid (AHAMA) was synthesized by modifying the carboxyl groups of hyaluronic acid (HA) with aldehyde and methacrylate groups. This modification was confirmed through 1H NMR spectroscopy, where the appearance of new peaks at 5.7 ppm and 6.1 ppm was attributed to the protons of the methacrylate C=C bonds (Fig. S6). When designing MS@LTO@TB, we capitalized on the spontaneous formation of Schiff bases between aldehyde and amino groups, a reaction that not only imparts high chemical stability to the system but also prolongs the retention of the drug within the nasal mucosa, enhancing its therapeutic effect.

By manipulating the flow rates of both the dispersed and continuous phases in the microfluidic system, the size of the hydrogel microspheres can be precisely adjusted [22,23]. Using LTO@TB and AHAMA as the dispersed phase and paraffin oil as the continuous phase, MS and MS@LTO@TB hydrogel microspheres were synthesized by precisely controlling these flow rates. Optical microscopy images revealed that MS@LTO@TB had a uniform diameter and spherical morphology (Fig. 2A and B). The particle sizes of MS and MS@LTO@TB are approximately 120 μm and 130 μm, respectively, indicating minimal size variation (Fig. 2I and J). FITC-labeled LTO@TB was used to assess the micro/nanostructural integration of LTO@TB within the MS. Laser confocal scanning microscopy (LCSM) confirmed the incorporation of FITC-labeled LTO@TB within the MS (Fig. 2C and D). SEM revealed that the hydrogel microspheres fabricated in this study had a porous microstructure (Fig. 2E–G). This porous architecture increased the specific surface area of the MS, improving the loading capacity for LTO@TB. Energy-dispersive X-ray spectroscopy (EDS) confirmed the successful loading of LTO@TB onto the MS (Fig. 2F–H). Fourier transform infrared (FTIR) spectroscopy confirmed the synthesis of MS@LTO@TB (Fig. 2K). A characteristic C=O peak at 1750 cm^{-1}, indicative of amide bonds, confirmed the modification of AHAMA [24]. The presence of symmetric and asymmetric stretching vibrations in the 1400-1500 cm^{-1} range verified the incorporation of LTO. The presence of peaks in the 1000-1250 cm^{-1} range (C-O and P=O stretching vibrations) and the 750-1000 cm^{-1} range (aromatic C-H bending vibrations) indicated the complex molecular structures of AHAMA, lecithin, and TB. X-ray photoelectron spectroscopy (XPS) confirmed the synthesis of MS@LTO@TB (Fig. 2L). The presence of a C 1s peak at 285 eV indicated the presence of AHAMA. The peak near 170 eV in the MS@Liposome sample was attributed to the phosphorus (P 2p) in phospholipids. The presence of a Ba 3d peak at 800 eV confirmed the integration of LTO. The peaks between 800 and 1100 eV were characteristic of complex organic structures, such as hydroxyl and methyl groups in TB. The positions and intensities of the characteristic peaks in the XPS spectra demonstrated the incorporation and surface modification of all the components in MS@LTO@TB.

In vitro degradation experiments revealed no significant changes in the morphology or appearance of MS@LTO@TB under bright-field microscopy during the first week. The structure remained dense, displaying a brownish-green hue and uniform surface texture with low light transmittance. MS@LTO@TB gradually developed hair-like textures at its periphery. Peripheral zone transmittance increased gradually, whereas the central area remained intact. From the fourth week, MS@LTO@TB transmittance markedly increased, with noticeable cracking and collapse at the boundaries. By the fifth week, MS@LTO@TB disintegrated, appearing as fragments under bright-field microscopy. By the sixth week, MS@LTO@TB was almost completely degraded and fragmented (Fig. 2M). The remaining mass of MS@LTO@TB was measured at different time points to further quantify the degradation profile. The results revealed a gradual decrease in MS

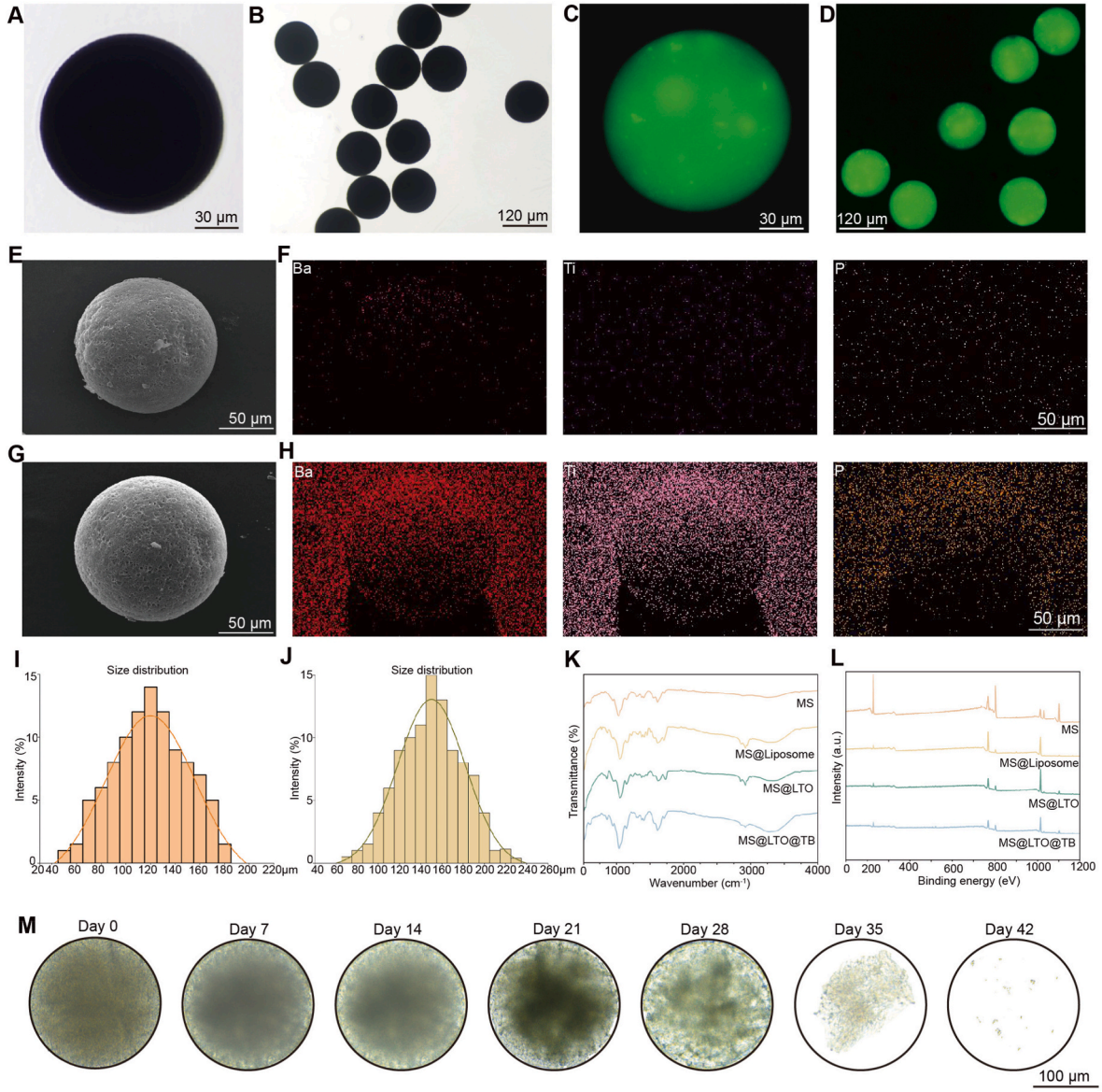

Fig. 2. Preparation and characterization of MS@LTO@TB. A, B) Morphology of MS@LTO@TB under bright-field microscopy: A) Individual MS@LTO@TB (Scale bar, 30 μm) and B) Dispersed MS@LTO@TB (Scale bar, 120 μm) under bright-field microscopy. C, D) LSCM images of C) individual MS@LTO@TB (Scale bar, 30 μm) and D) Dispersed MS@LTO@TB (Scale bar, 120 μm). E) SEM image of MS. Scale bar, 50 μm. F) EDX surface-scan element distribution of Ba, Ti and PS of MS. Scale bar, 50 μm. G) SEM image of MS@LTO@TB. Scale bar, 50 μm. H) EDX surface-scan element distributions of Ba, Ti and O in MS@LTO@TB. Scale bar, 50 μm. I) Size distribution of MS. J) Size distribution of MS@LTO@TB. K) FTIR spectra of MS, MS@Liposome, MS@LTO and @MS@LTO@TB. L) XPS regions of MS, MS@Liposome, MS@LTO and @MS@LTO@TB. M) Microscopy images showing the morphological changes in MS@LTO@TB over time. Scale bar, 50 μm. The data are presented as mean ± SD (n = 3) for each group.

mass over time, from 45 ± 2 % in the fourth week to 15 ± 5 % in the seventh week (Fig. S7). The controlled release of TB from MS@LTO@TB in vitro was examined. In PBS with hyaluronidase, the cumulative amount of TB released reached 33 % by the 14th day, indicating that LTO@TB within MS can achieve prolonged and sustained release of TB. The controlled release of TB from MS@LTO@TB under ultrasonic stimulation in vitro was investigated. In PBS with hyaluronidase, the cumulative amount of TB released reached 42 % by the 14th day, suggesting that US enhances the sustained release of TB in vitro (Fig. S8).

3.3. Study of the adhesion of MS@LTO@TB to the nasal mucosa

The gold standard for evaluating the safety of nasal formulations is analyses of ciliary movement on the toad palate, which closely mimics ciliary activity and mucus secretion in the nasal cavity [9,25]. We thus evaluated ciliary movement on the toad palate to evaluate the adhesion capability of MS@LTO@TB (Fig. S9). The results revealed that the mucosal retention times for HAMA@LTO@TB and MS@LTO@TB were 350 ± 15.5 s and 1850 ± 30.33 s, respectively, with ciliary clearance rates of 0.15 ± 0.05 mm/min and 0.02 ± 0.01 mm/min, respectively. These results demonstrate that MS@LTO@TB exhibits a significantly prolonged mucosal retention time and a markedly reduced nasal ciliary clearance rate, indicating excellent nasal mucosal adhesion.

3.4. Investigation of the protective effects of MS@LTO@TB on BV-2 cells

To verify whether MS@LTO@TB influences the inflammatory niche after IS in vitro, MS@LTO@TB was cocultured with BV-2 cells stimulated with lipopolysaccharide (LPS), followed by US irradiation to induce a piezoelectric effect (Fig. 3A). The US parameters were as

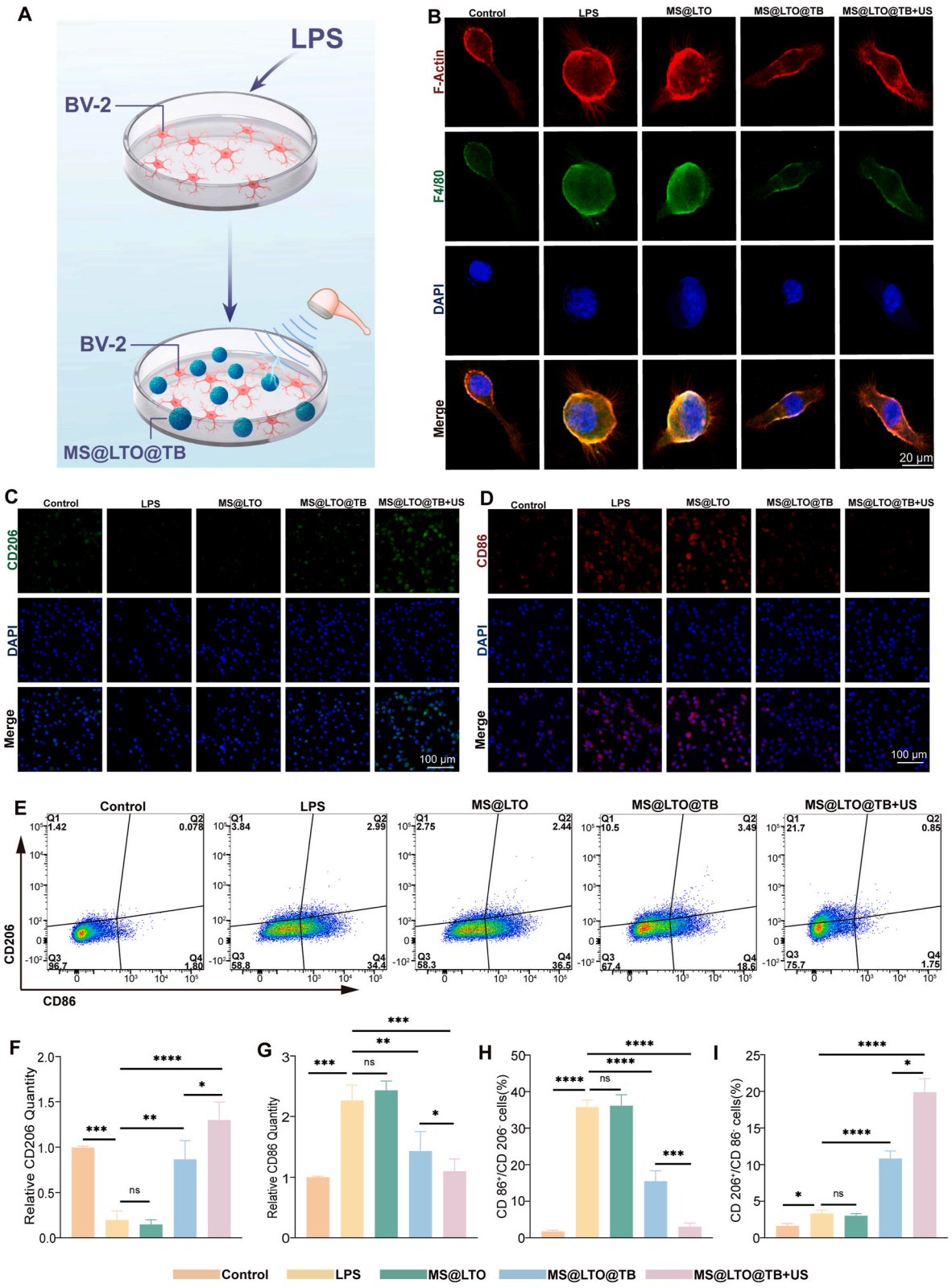

Fig. 3. Selective phenotypic transformation of BV-2 cells by MS@LTO@TB. A) Schematic illustration of the cell treatment protocols. B) Influence of different treatments on the IF intensity of BV-2 cells. Scale bar, 20 μm. C, D) Representative images of IF staining for CD86 and CD206 after different treatments. Scale bar, 100 μm. E) Representative flow cytometry images showing CD86 and CD206 expression after different treatments. F, G) Percentage of cells positive for CD86 and CD206 after IF staining (n = 3). H, I) Quantitative analysis of positive cells via flow cytometry. n = 3 for each group. Data are presented as mean ± SD (n = 3) for each group. *P < 0.05, **P < 0.01, ***P < 0.001, ****P < 0.0001.

follows: 1 W/cm^2, 1 MHz, 50 % duty cycle, and 60 s. Before the cellular experiments, live/dead assays were used to assess the biocompatibility of the hydrogel microsphere with BV-2 cells. As shown in Fig. S10, no cytotoxicity was detected in any group. To investigate the effects of MS@LTO@TB on BV-2 cells, the cytoskeleton of BV-2 cells was stained with Alexa Fluor 555-phalloidin. F4/80, a marker for mature macrophages, was used to specifically label BV-2 cells. DAPI was used to stain BV-2 cell nuclei, and morphological differences among groups were observed via LCSM (Fig. 3B). In the control group, BV-2 cells presented a typical resting-state morphology with small, spoon-shaped cell bodies. In sharp contrast, the cells in the LPS and MS@LTO groups had an amoeboid shape with flattened cell bodies and an increased number of pseudopodia. BV-2 cells in the MS@LTO@TB and MS@LTO@TB + US groups presented a spindle-shaped morphology. Phenotypic changes in BV-2 cells were analyzed through immunofluorescence (IF). The LPS group exhibited a significantly higher number of CD86$^+$ cells and a lower number of CD206$^+$ cells compared to the control group. No significant differences were found between the MS@LTO and LPS groups. In contrast, the MS@LTO@TB group showed a substantial reduction in CD86$^+$ cells and a significant increase in CD206$^+$ cells relative to the LPS group. Under US stimulation, the piezoelectric properties of MS@LTO@TB further enhanced the reduction in CD86$^+$ cells and promoted an increase in CD206$^+$ cells (Fig. 3C, D, F, G). It is hypothesized that the piezoelectric effect activates calmodulin-dependent kinases (CaMKs) and calcineurin. The activation of CaMK and calcineurin is capable of inhibiting proinflammatory signaling pathways, such as the NF-κB pathway, thereby reducing the expression of pro-inflammatory cytokines [26]. The activation of CaMK and calcineurin can enhance anti-inflammatory responses by activating transcription factors such as CREB, thereby promoting the expression of anti-inflammatory cytokines like IL-10 and TGF-β, and subsequently fostering BV-2 cells a neuroprotective state [25,27]. Flow cytometry analysis revealed that the LPS group had a greater proportion of CD86$^+$ cells and a lower proportion of CD206$^+$ cells than did the control group. No significant differences were found between the MS@LTO and control groups. Compared with the LPS group, the MS@LTO@TB group presented fewer CD86$^+$ cells and more CD206$^+$ cells. Under US stimulation, the proportions of CD86$^+$ and CD206$^+$ cells were similar to those in the control group (Fig. 3E–H, I).

In summary, the MS@LTO@TB l, with its precisely designed composite structure, exhibits excellent piezoelectric properties, enabling it to induce a direct piezoelectric effect under US irradiation. Based on experimental results, we hypothesize that the piezoelectric effect activates the CaMKs and calcineurin signaling pathways within BV-2 cells, thereby inhibiting the activity of the pro-inflammatory transcription factor NF-κB and reducing the expression of the pro-inflammatory marker CD86. Meanwhile, the activation of CaMKs and calcineurin enhances the phosphorylation of the transcription factor CREB, boosting the anti-inflammatory response and increasing the expression of anti-inflammatory cytokines IL-10 and TGF-β. This series of molecular mechanisms promotes the transformation of BV-2 cells into an anti-inflammatory phenotype. Furthermore, MS@LTO@TB has demonstrated potential in modulating the inflammatory microenvironment even without US stimulation, and under US activation, its anti-inflammatory effect is significantly enhanced, alleviating LPS-induced inflammation and creating a microenvironment conducive to neuroprotection and regeneration. Therefore, the MS@LTO@TB material, through its unique structural-functional synergy, effectively mitigates the microenvironment detrimental to neural regeneration, providing an ideal condition for protecting neurons damaged after ischemic stroke and thrombolysis.

3.5. Investigation of the mechanism by which the key component of MS@LTO@TB, TB, reprograms BV-2 cells

After thrombolysis for IS, the balance of microglial activation states is disrupted, resulting in a predominance of pro-inflammatory responses and excessive release of inflammatory cytokines. This imbalance primarily causes extensive neuronal apoptosis in the ischemic penumbra of the brain. TB is the most abundant saponin monomer in Timosaponin, which is derived from the dried rhizomes of *Anemarrhena asphodeloides* [28]. A variety of research has highlighted the diverse therapeutic benefits of TB, including its anti-inflammatory, antioxidant, and antidepressant properties [29–32]. However, research on the application of TB to treat IS after thrombolysis is currently limited. This study provides theoretical support for the future use of TB after thrombolysis in IS patients. LPS can activate microglia, shifting them from a homeostatic state to a pro-inflammatory state, which leads to the excessive secretion of inflammatory cytokines and subsequent neuronal apoptosis [33]. Conversely, anti-inflammatory microglia can adopt a neuroprotective state by secreting anti-inflammatory cytokines and neurotrophic factors, thereby exerting neuroprotective and regenerative effects. Therefore, we cocultured MS@LTO@TB with BV-2 cells to assess whether TB can modulate the shift of BV-2 cells from a pro-inflammatory to an anti-inflammatory activation state. Compared to the control group, the LPS-treated group showed a rise of approximately 90 pg/ml and 80 pg/ml in TNF-α and IL-1β concentrations respectively. Compared with LPS, MS@LTO@TB reduced TNF-α and IL-1β levels by approximately 85 pg/ml and 81 pg/ml, respectively, while increasing the levels of the anti-inflammatory cytokines IL-10 and Arg-1 by approximately 20 pg/ml and 28 pg/ml, respectively. There were no significant differences observed between the MS@LTO group and the MS@LTO@TB group (Fig. S11 B, C, D, E). Treatment with MS@LTO@TB promoted BV-2 cells toward a neuroprotective activation state.

Saponins, recognized as activators of peroxisome proliferator-activated receptor gamma (PPARγ), have demonstrated the ability to reduce inflammatory responses and prevent neuronal cell death in mouse models of Alzheimer's disease [34–36]. TB inhibits the pro-inflammatory activation of microglia and promotes their transition to a neuroprotective state by suppressing NF-κB p65 phosphorylation and MAPK p38 nuclear translocation [37]. In this study, Western blot analysis confirmed that, compared with the blank treatment, LPS stimulation decreased PPARγ expression, whereas MS@LTO@TB significantly increased PPARγ expression. Western blot analysis revealed that, compared with the blank treatment, LPS stimulation decreased PPARγ expression, whereas MS@LTO@TB significantly increased it.

In conclusion, the key component TB in MS@LTO@TB, as a PPARγ receptor agonist, successfully regulated the activation state of BV-2 cells, shifting them from a pro-inflammatory state to a neuroprotective state. TB inhibited the phosphorylation of NF-κB p65 and the nuclear translocation of MAPK p38, blocking pro-inflammatory signaling pathways, which significantly reduced the expression of pro-inflammatory cytokines TNF-α and IL-1β, while simultaneously upregulating the levels of anti-inflammatory factors IL-10 and Arg-1. These functional characteristics of MS@LTO@TB demonstrate significant potential for its application in the treatment of IS post-thrombolysis, and provide theoretical support for its use in other neuroinflammatory-related diseases.

3.6. In vitro neuroprotective effects of MS@LTO@TB

Beyond reconstructing the local niche, inducing the regeneration of damaged neurons after thrombolysis remains a critical challenge in IS. PC-12 cells, which are derived from the adrenal medulla of rat with pheochromocytoma, are widely used in neuroscience research, particularly for studying neurotoxicity, neuroprotection, and neuroinflammation [38,39]. Therefore, cocultured BV-2 and PC-12 cells were used as an in vitro model to evaluate the protective effects of MS@LTO@TB on neuronal proliferation and neurite outgrowth.

To confirm whether the effect of MS@LTO@TB in reprogramming microglia can protect PC-12 cells cocultured with LPS-stimulated BV-2 cells, BV-2 cells and MS@LTO@TB cells were seeded in the upper chamber of a Transwell system, while PC-12 cells were placed in the bottom chamber (Fig. 4A). PC-12 cell apoptosis was assessed via flow

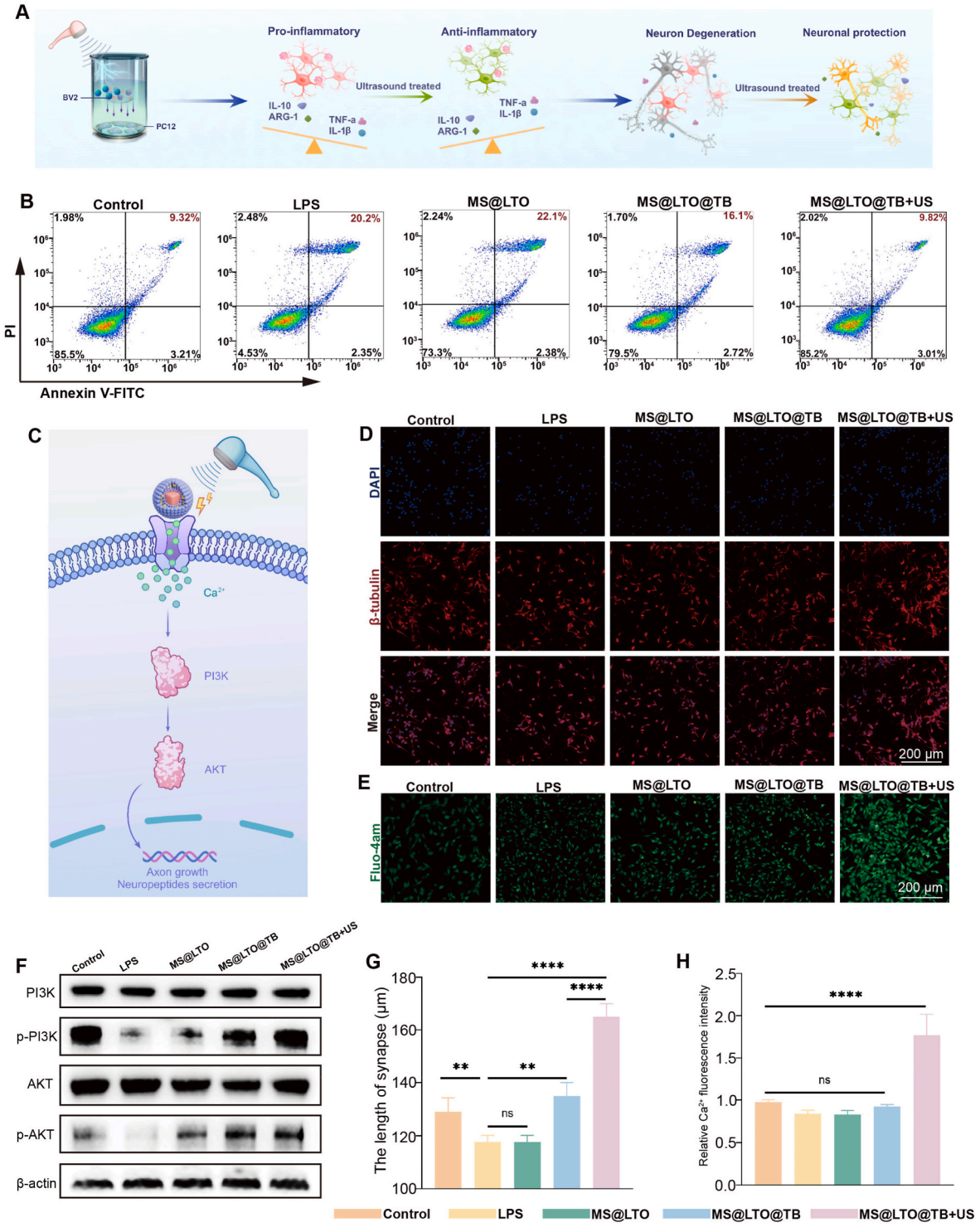

Fig. 4. MS@LTO@TB protects injured PC-12 cells. A) Schematic illustration of cell treatment protocols and the mechanisms of microglial reprogramming, changes in the expression of different factors and neuronal protection. B) Representative flow cytometry images showing the apoptosis of PC-12 cells subjected to different treatments. C) Schematic of the neurogenesis mechanism. D) IF images showing the axon stretching of PC-12 cells. Scale bar, 200 μm. E) IF images of the intracellular Ca2+ concentration in PC-12 cells. Scale bar, 200 μm. F) Western blot analysis of PI3K, p-PI3K, AKT, p-AKT and β-tubulin expression. G) Measurement and quantification of the synapse length. (n = 3). H) Quantification of the relative Ca2+ fluorescence intensity. n = 3 for each group. are presented as mean ± SD (n = 3) for each group. *P < 0.05, **P < 0.01, ***P < 0.001, ****P < 0.0001.

cytometry. As shown in Fig. 4B, the LPS group exhibited a significant increase in apoptosis. There were no significant variations between the MS@LTO and LPS groups. As previously demonstrated, MS@LTO@TB strongly induced BV-2 cell reprogramming, downregulated proinflammatory cytokines and upregulated anti-inflammatory cytokines. Consequently, flow cytometry revealed a reduction in the percentage of apoptotic cells in the MS@LTO@TB group. Under US stimulation, the apoptosis rate of PC-12 cells approached that of the control group. These findings suggest that MS@LTO@TB has potential neuroregenerative properties.

Axon length is considered the gold standard for evaluating the effects of different materials on neural regeneration. IF staining for β-tubulin was performed on PC-12 neurons. The average axon length in the control group was approximately 130 μm, whereas in the LPS and MS@LTO groups, it was approximately 115 μm. The MS@LTO@TB group presented an axon length comparable to that of the control group, i.e., approximately 130 μm. Under US stimulation, MS@LTO@TB enhanced axon growth, with the axon length reaching approximately 165 μm (Fig. 4D–G). These results indicate that the piezoelectric effect of MS@LTO@TB under US stimulation significantly promotes axon growth in damaged neurons. Ca^{2+} plays a crucial role in neuronal cells, participating in signaling processes such as neurotransmitter release, membrane excitability, depolarization, and synaptic activity regulation. The activation of voltage-gated Ca^{2+} channels is essential for neuronal proliferation, migration, and neurite outgrowth [40]. The PI3K-AKT pathway is critical for regulating intracellular oxidative stress, which is closely related to CIRI. Voltage-gated Ca^{2+} channels phosphorylate downstream proteins in the PI3K-AKT pathway, regulating neuronal activity and promoting axon growth [41]. To further explore how the piezoelectric effect promotes neural regeneration under US stimulation, Ca^{2+} concentrations in PC-12 cells were measured via the calcium indicator Fluo 4-AM. There were no significant differences in intracellular Ca^{2+} levels among the control, LPS, MS@LTO, and MS@LTO@TB groups. However, the MS@LTO@TB + US group presented significantly higher intracellular Ca^{2+} concentrations than the other groups did, which was consistent with previous findings (Fig. 4E–H). Western blot analysis indicated that MS@LTO@TB promotes axon growth through phosphorylation of PI3K-AKT pathway components.

In summary, we established a co-culture model of BV-2 cells and PC-12 cells to investigate the neuroprotective and neuroregenerative effects of MS@LTO@TB after IS thrombolysis. The results showed that MS@LTO@TB significantly alleviated PC-12 cell apoptosis and, under US stimulation, promoted axonal growth. Notably, under US stimulation, the axon length in the MS@LTO@TB group was restored to levels close to the control group, whereas the LPS group and MS@LTO group did not achieve this effect. This indicates that MS@LTO@TB has a significant advantage in regulating the activation state of BV-2 cells, inhibiting inflammation, and promoting neuroregeneration. Further studies revealed that MS@LTO@TB, through the electrical signals generated under US stimulation, increased intracellular calcium ion concentrations and activated the PI3K-AKT signaling pathway, thereby promoting neuronal proliferation and axonal growth. These results suggest that MS@LTO@TB has remarkable neuroprotective effects and facilitates neuroregeneration by modulating intracellular calcium ions and the PI3K-AKT pathway. The therapeutic strategy of MS@LTO@TB provides new insights for the treatment of CNS diseases, such as acute ischemic stroke.

3.7. *In vivo targeting and biodistribution of MS@LTO@TB*

To evaluate the retention time of MS@LTO@TB in the brain, LTO@TB was labeled with DIR. MS@LTO@TB/DIR was administered intranasally to C57 BL/6J mice for in vivo fluorescence imaging, and US was applied daily. In vivo fluorescence imaging was performed on days 1, 3, 5, 7, and 14 after administration. The fluorescence intensity of MS@LTO@TB increased significantly starting from the first day, reaching its peak on the third day and the elevated fluorescence intensity persisted until the fourteenth day. In contrast, the fluorescence intensity in the LTO@TB group decreased significantly by the seventh day, with only faint signals detectable by the fourteenth day (Fig. 5A and B). Subsequent ex vivo imaging of brain tissues and other organs indicated that MS@LTO@TB had a longer administration window than LTO@TB did (Fig. 5C and D). MS@LTO@TB/DIR may partially accumulate in the lungs through the respiratory tract during intranasal administration. To further evaluate the clearance process of these nanoparticles in the lungs, ex vivo fluorescence imaging experiments were conducted on day 21 and day 30 post-administration. The results showed that, on day 21, while certain fluorescence signals were still

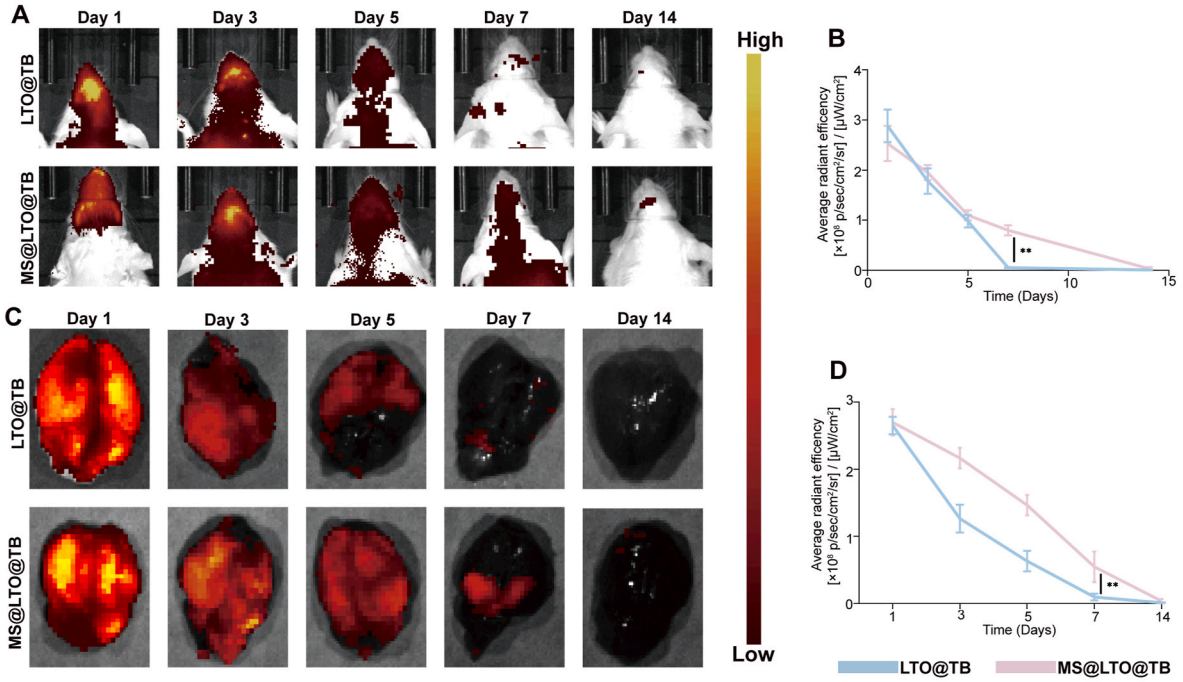

Fig. 5. In vivo targeting and biodistribution of MS@LTO@TB. A, B) Real-time fluorescence imaging of mice and quantification of the fluorescence intensity after nasal administration of LTO@TB and MS@LTO@TB. C) Ex vivo fluorescence imaging of the brains of sacrificed mice after intranasal administration of LTO@TB and MS@LTO@TB. D) Ex vivo fluorescence imaging of organs collected from sacrificed mice after intranasal administration of LTO@TB and MS@LTO@TB. E) Ex vivo fluorescence imaging of the brains of sacrificed mice and quantification of the fluorescence intensity after intranasal administration of LTO@TB and MS@LTO@TB. n = 5 for each group. are presented as mean ± SD (n = 5) for each group. **P < 0.01.

detectable in the lungs, their intensity had significantly decreased compared to day 14, indicating that the nanoparticles were gradually being cleared by the body. By day 31, only very weak fluorescence signals were detected in the lungs (Fig. S12), suggesting that MS@LTO@TB had been nearly completely cleared from the lungs. Additionally, histopathological analysis of the lung tissue from mice on day 31 revealed no significant inflammation, tissue damage, or other pathological changes (Fig. S13), further confirming the excellent biocompatibility and safety of MS@LTO@TB.

Overall, the aldehyde groups in MS@LTO@TB spontaneously form Schiff bases with the amines on the nasal mucosa, which helps maintain its high stability and prolonged retention within the nasal mucosal environment. In vivo imaging results indicate that MS@LTO@TB reaches its peak concentration within three days after administration and maintains this level until day fourteen, significantly outperforming the retention capability of LTO@TB. Although some LTO@TB can enter the lungs via the respiratory tract, this non-targeted distribution has a limited impact on its brain-targeting effect. The efficient brain-targeting and sustained retention characteristics of MS@LTO@TB not only enhance its potential therapeutic efficacy in the treatment of IS post-thrombolysis but also provide a highly feasible nanoparticle carrier platform for targeted drug delivery in central nervous system diseases.

3.8. MS@LTO@TB reduces the brain infarct volume and restores neurological function in vivo

Owing to the excellent brain-targeting ability of MS@LTO@TB, its in vivo therapeutic effects were further investigated. Mice were randomly assigned to five groups, and an MCAO/R model was established. The mice received intranasal administration of saline, intranasal administration of MS@LTO, intranasal administration of MS@LTO@TB, or intranasal administration of MS@LTO@TB combined with US stimulation according to the experimental design (Fig. 6A). On the 14th day, the open field test (OFT) was conducted to assess the cognitive function and memory of the MCAO/R model mice (Fig. 6B). Compared with the control group, the MCAO/R group exhibited less activity in the central area, with a significantly lower number of entries into the central area and a shorter duration spent and distance traveled in the central area. No

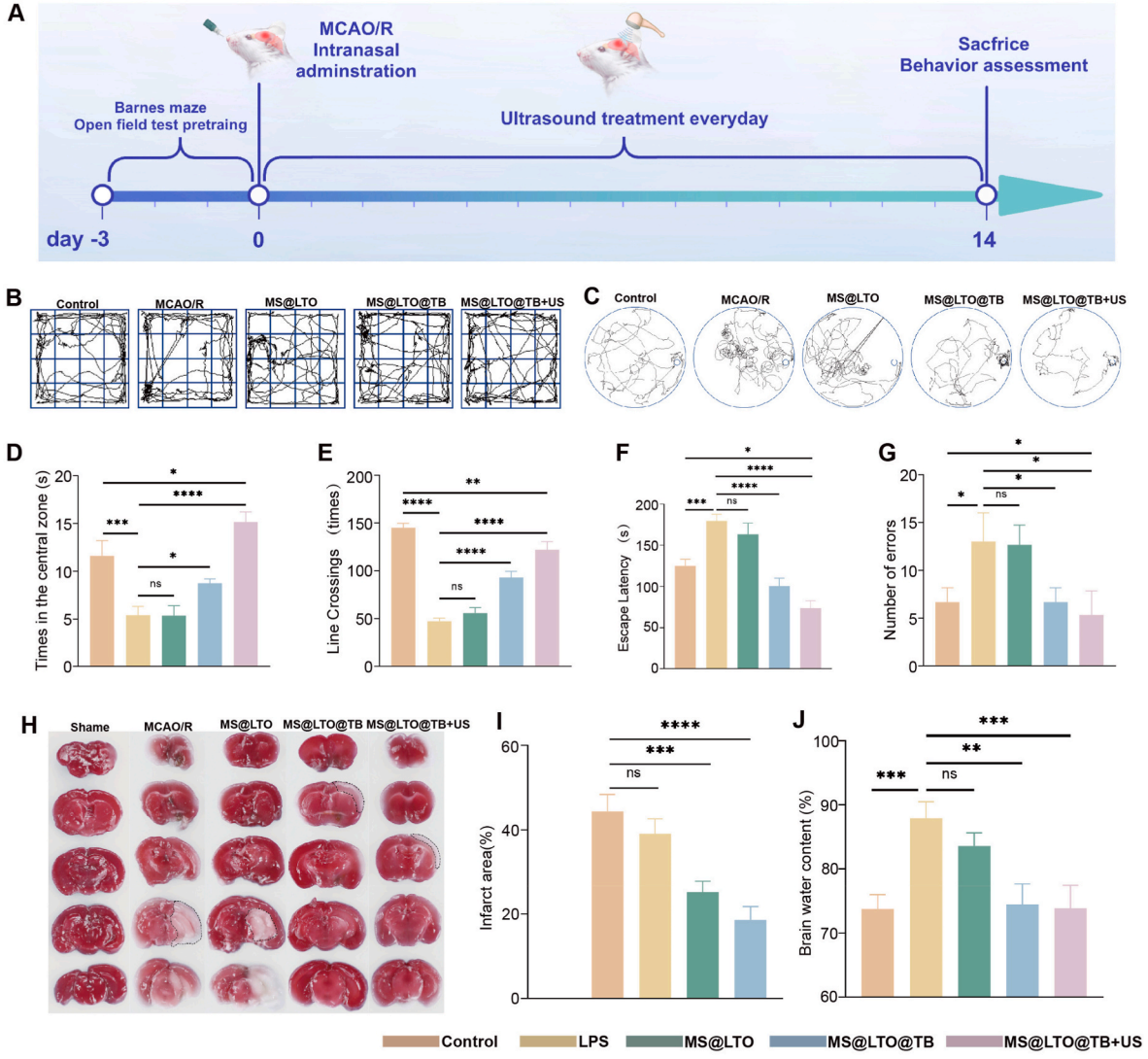

Fig. 6. MS@LTO@TB reduces the brain infarct volume and restores neurological function in vivo. A) Schematic of the in vivo experiment involving model mice. B) Results of the OFT, which was used to assess mouse behavior, after different treatments. C) The results of the Barnes maze, which was used to assess mouse behavior, after different treatments. D, E) The average time spent in the central zone and number of line crossings for each group of mice in the OFT. F, G) The average escape latency and number of errors for each group of mice in the Barnes maze test. H) TTC staining images of mouse brain tissues after different treatments. I) Analysis of the infarct size from TTC-stained images.J) Analysis of water content in the ischemic brain after different treatments. n = 5 for each group. are presented as mean ± SD (n = 5) for each group. ns: no significance; *P < 0.05, **P < 0.01, ***P < 0.001, ****P < 0.0001.

significant differences were observed between the MS@LTO group and the MCAO/R group. However, treatment with MS@LTO@TB significantly improved these indicators. These findings suggest that MS@LTO@TB positively affects cognitive function and memory in mice after MCAO/R. The Barnes maze test was used to evaluate cognitive function in mice after MCAO/R (Fig. 6C). On the 14th day, the path length, escape latency, and number of errors were analyzed to assess spatial learning ability. The results indicated that, in comparison to the mice in the control group, MCAO/R model mice required more attempts and traveled a longer distance to find the escape hole. No significant differences were observed between the MS@LTO and MCAO/R groups. In contrast, MS@LTO@TB-treated mice presented significantly reduced spatial learning deficits, requiring a shorter amount of time to find the escape hole and making fewer errors. MS@LTO@TB + US treatment markedly increased spontaneous exploratory behavior in new environments, restoring it to normal levels (Fig. 6F and G). The Barnes maze test results suggested that MS@LTO@TB + US promotes long-term neurological function recovery after MCAO/R. After behavioral testing, TTC staining was performed to evaluate brain infarct volumes in MCAO/R model rats subjected to various treatments (Fig. 6H). In comparison to the MCAO/R group, the infarct volumes were reduced to 23 % and 16 % in the MS@LTO@TB and MS@LTO@TB + US groups respectively. The MCAO/R and MS@LTO groups showed no noteworthy differences (Fig. 6I). To evaluate the impact of different treatments on cerebral edema in MCAO/R model mice, brain water content was measured [42]. The brain water content was notably decreased in the MS@LTO@TB and MS@LTO@TB + US groups when compared to the MCAO/R group. However, there was no significant difference between the MCAO/R and MS@LTO groups (Fig. 6J). In summary, MS@LTO@TB significantly improved cognitive function and memory in MCAO/R model mice via nasal administration, demonstrating its excellent brain-targeting ability and neuroprotective potential. In the OFT and Barnes maze test, mice in the MS@LTO@TB group showed significant improvements in central zone activity, spatial learning, and memory tasks, indicating its effectiveness in promoting neural function recovery. This result is likely closely related to its ability to regulate microglial activation, modulate inflammatory responses, and promote neuronal regeneration. Furthermore, the combined application of ultrasound stimulation further enhanced the therapeutic effect of MS@LTO@TB, consistent with the results from in vitro experiments. TTC staining and brain edema analysis further confirmed that the brain infarct volume and brain edema were significantly reduced in the MS@LTO@TB and MS@LTO@TB + US treatment groups, suggesting that the treatment effectively reduced brain damage and alleviated brain edema, thus improving the microenvironment after neuron injury. Overall, MS@LTO@TB exhibits significant neuroprotective effects, particularly in the synergistic effect of ultrasound stimulation, and can significantly promote recovery of neural function after acute ischemic stroke, demonstrating broad clinical application potential.

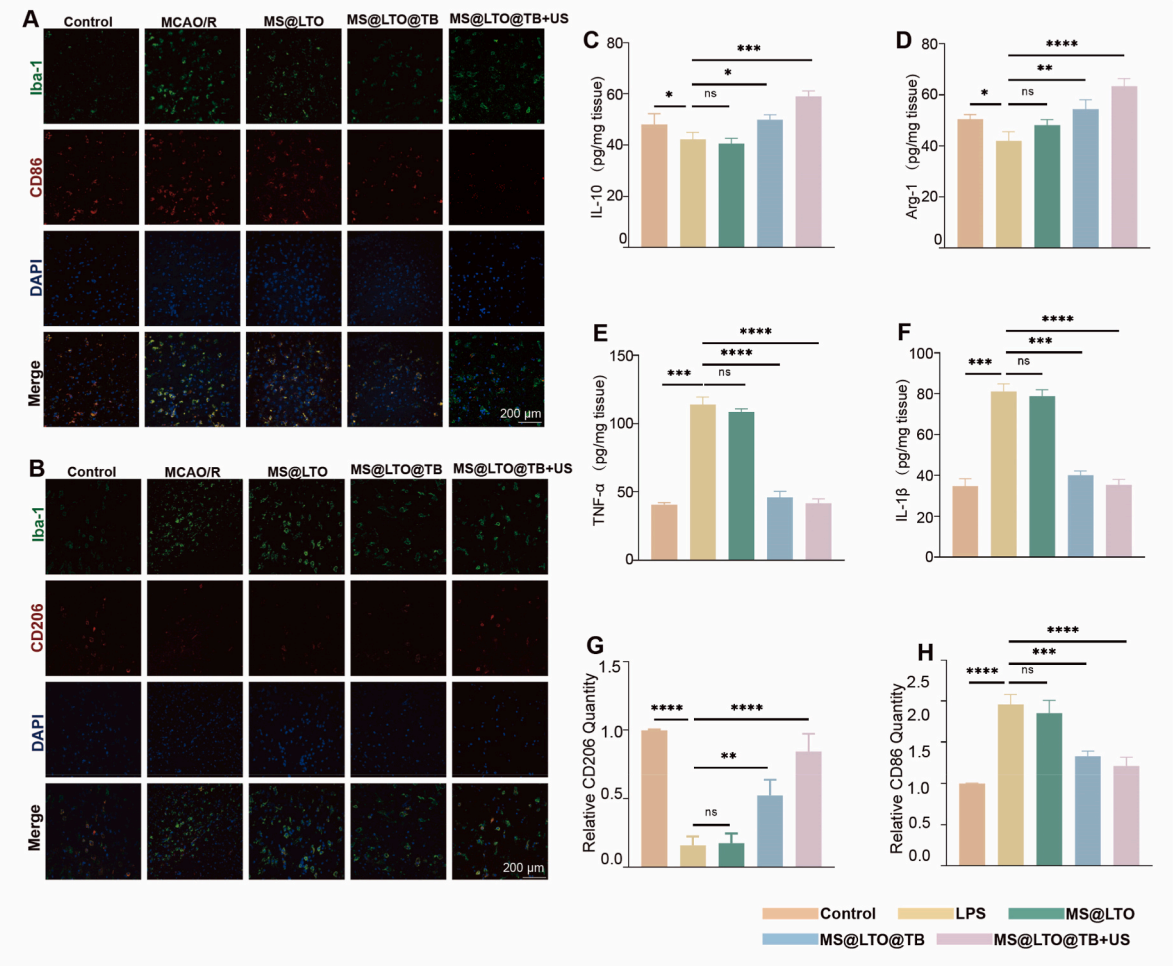

Fig. 7. In vivo anti-inflammatory effects of MS@LTO@TB. A) Images of costaining for Iba-1 and CD86 on the injured side of the brain in different groups. Scale bar, 200 μm. B) Images of costaining for Iba-1 and CD206 on the injured side of the brain in different groups. Scale bar, 200 μm. C, D, E, F) Expression of IL-10, Arg-1, TNF-α and IL-1β in the ischemic brain after different treatments. G, H) Statistical analysis of Iba-1/CD206 and Iba-1/CD86 costaining according to IF. n = 5 for each group. The data are presented as mean ± SD (n = 5) for each group. ns. No significance, *P < 0.05, **P < 0.01, ***P < 0.001, ****P < 0.0001.

3.9. Anti-inflammatory effects of MS@LTO@TB in vivo

In comparison to the MCAO/R group, the MS@LTO@TB and MS@LTO@TB + US groups exhibited significantly reduced levels of reactive oxygen species (ROS), confirming the effective free radical scavenging ability of MS@LTO@TB (Fig. S12). The inflammatory response in ischemic brain tissue was assessed by measuring the amounts of various cytokines, including the anti-inflammatory IL-10 and Arg-1, as well as the proinflammatory TNF-α and IL-1β, employing an ELISA-based approach. Elevated proinflammatory cytokine levels were observed in the MCAO/R group relative to the control group. However, in the MS@LTO@TB group, there was a marked reduction in proinflammatory cytokine concentrations and a noticeable increase in anti-inflammatory cytokines when compared to the MCAO/R group. These results are consistent with the in vitro findings, indicating that MS@LTO@TB can improve the prognosis of CIRI (Fig. 7C, D, E, F). After MCAO/R, microglial activation and their functional polarization significantly contribute to neuroinflammation. Microglial subsets exhibiting pro-inflammatory and anti-inflammatory activation states in the ischemic penumbra were identified by double immunostaining with Iba-1 and CD86 (for proinflammatory activation) or Iba-1 and CD206 (for anti-inflammatory activation). The results revealed increased CD86 expression and decreased CD206 expression in the MCAO/R group, with no significant differences between the MS@LTO and MCAO/R groups. The MS@LTO@TB treatment resulted in reduced expression of the proinflammatory marker CD86 and elevated expression of the anti-inflammatory marker CD206. Upon of US treatment, the MS@LTO@TB + US group presented a further decrease in CD86 expression and an increase in CD206 expression (Fig. 7A and B).

In summary, MS@LTO@TB demonstrates excellent antioxidant and anti-inflammatory properties, proving its potential therapeutic value in CIRI. Oxidative stress is a key contributor to CIRI, where excessive free radicals not only directly lead to excessive apoptosis of normal cells but also exacerbate neuroinflammation by activating pro-inflammatory pathways. In this study, MS@LTO@TB effectively scavenged free radicals, significantly reducing ROS levels and thereby alleviating oxidative stress damage. Furthermore, MS@LTO@TB improved the physiological microenvironment of brain tissue by reducing the levels of pro-inflammatory cytokines (TNF-α, IL-1β) and increasing the expression of anti-inflammatory factors (IL-10, Arg-1). Additionally, MS@LTO@TB regulated the activation state of microglial cells, decreasing the expression of pro-inflammatory marker CD86 and increasing the expression of anti-inflammatory marker CD206, thereby inhibiting excessive neuroinflammatory responses. Importantly, the electro-pharmacological coupling effect in response to US further improved the therapeutic outcome. These results indicate that MS@LTO@TB has the potential to alleviate the pathological effects of ischemic brain injury by regulating neuroinflammation, presenting a promising therapeutic approach for CIRI.

3.10. Neuroprotective and neurorestorative effects of MS@LTO@TB in vivo

To assess the protective effects of MS@LTO@TB in MCAO/R model mice, hematoxylin and eosin (HE) staining was performed to examine the morphology of the ischemic penumbra, while Nissl staining was used to evaluate neuronal structure. The HE staining results showed that in the control group, the ischemic penumbra displayed a well-preserved structure, normal cell morphology, uniform staining, and centrally positioned nuclei. In contrast, the MCAO/R group exhibited significant cellular disruption, characterized by a disordered arrangement of cells, decreased neuronal density, abnormal cell swelling, nuclear condensation, and loose intercellular spaces. The MS@LTO@TB group showed significant improvements compared to the MCAO/R group, with better-preserved cell morphology, less nuclear condensation, and an increased number of intact cells. In the MS@LTO@TB + US group, the number of normal cells further increased, and lighter uniform staining and mild nuclear swelling were observed. Nissl staining revealed normal neuronal morphology, orderly arrangement of cells, and abundant Nissl bodies in the control group. In the MCAO/R group, neuronal morphology was abnormal, with a reduced number of cells, disorganized cellular arrangement, and significantly fewer Nissl bodies. Compared with that in the MCAO/R group, neuronal morphology in the MS@LTO@TB group was markedly improved, with uniform staining and more Nissl bodies. In the MS@LTO@TB + US group, the number of normal cells further increased, exhibiting a spreading morphology and more Nissl bodies (Fig. 8A). These data indicate that MS@LTO@TB effectively inhibits neuronal apoptosis, restores neuronal morphology and structure, and alleviates infarction, neurological deficits, and motor impairments induced by ischemia–reperfusion in MCAO/R model mice.

To further validate the neuroprotective and neuroregenerative effects of MS@LTO@TB, we employed Tuj1 and MAP2 staining for evaluation (Fig. 8B). In the MCAO/R model, there was a marked decrease in the number of $Tuj1^+$ cells within the peri-infarct area, indicating that damaged neurons were unable to spontaneously mature post-ischemia. Specifically, the MCAO/R group exhibited a markedly lower number of $Tuj1^+$ cells compared to the MS@LTO@TB group, which showed a significant increase in $Tuj1^+$ cell numbers. This suggests that MS@LTO@TB improves the microenvironment, promoting the early repair and survival of neurons, particularly in the peri-infarct region. It is noteworthy that Tuj1, as a classical marker of early neuronal differentiation, is typically associated with the activation state of neurogenesis, especially during the survival of newly generated neurons and the initial phases of repair. However, Tuj1-labeled cells are predominantly early-stage recovering neurons that have not yet fully matured. Therefore, while $Tuj1^+$ cells can reflect the process of neurogenesis, they alone cannot conclusively demonstrate that neurons have undergone complete recovery or regeneration from injury, particularly regarding axonal regeneration. To overcome this limitation, our study employed a co-staining strategy using both Tuj1 and MAP2 to comprehensively assess different stages of neural repair. MAP2, as a marker of mature neurons, is highly expressed in dendrites and cell bodies. Changes in MAP2 expression typically reflect the structural recovery and maturation of neurons. By co-staining with Tuj1 and MAP2, we were able to distinguish between different stages of neuronal recovery. In the peri-infarct region, $Tuj1^+/MAP2^-$ cells generally represent neurons in the recovery process, potentially still undergoing synaptic reconstruction and axonal growth. In contrast, neurons that are double-positive for Tuj1 and MAP2 likely indicate those that have undergone initial structural repair and are approaching maturity. This co-staining strategy not only effectively differentiates between various developmental stages of newly generated neurons but also provides a more detailed perspective on the maturation and repair processes of neurons. Notably, MAP2 expression was significantly higher in both the MS@LTO@TB and MS@LTO@TB + US groups compared to the MCAO/R group, whereas no significant difference was observed between the MS@LTO group and the MCAO/R group (Fig. 7G and H). This indicates that MS@LTO@TB treatment effectively promotes the structural repair and maturation of neurons, particularly during dendritic and synaptic reconstruction. Additionally, the MAP2 expression level in the MS@LTO@TB + US group was higher than that in the MS@LTO@TB group, which may be attributed to the enhanced structural repair and functional recovery of neurons facilitated by electrical stimulation under US treatment.

Overall, these results indicate that MS@LTO@TB combined with US treatment significantly reduced the brain infarct volume and cerebral edema in MCAO/R model mice, lowered ROS levels, and improved cognitive function and memory. By modulating proinflammatory and anti-inflammatory cytokine levels, it promoted neurogenesis, ameliorated neuroinflammation, and enhanced neurological recovery after CIRI, demonstrating remarkable therapeutic efficacy.

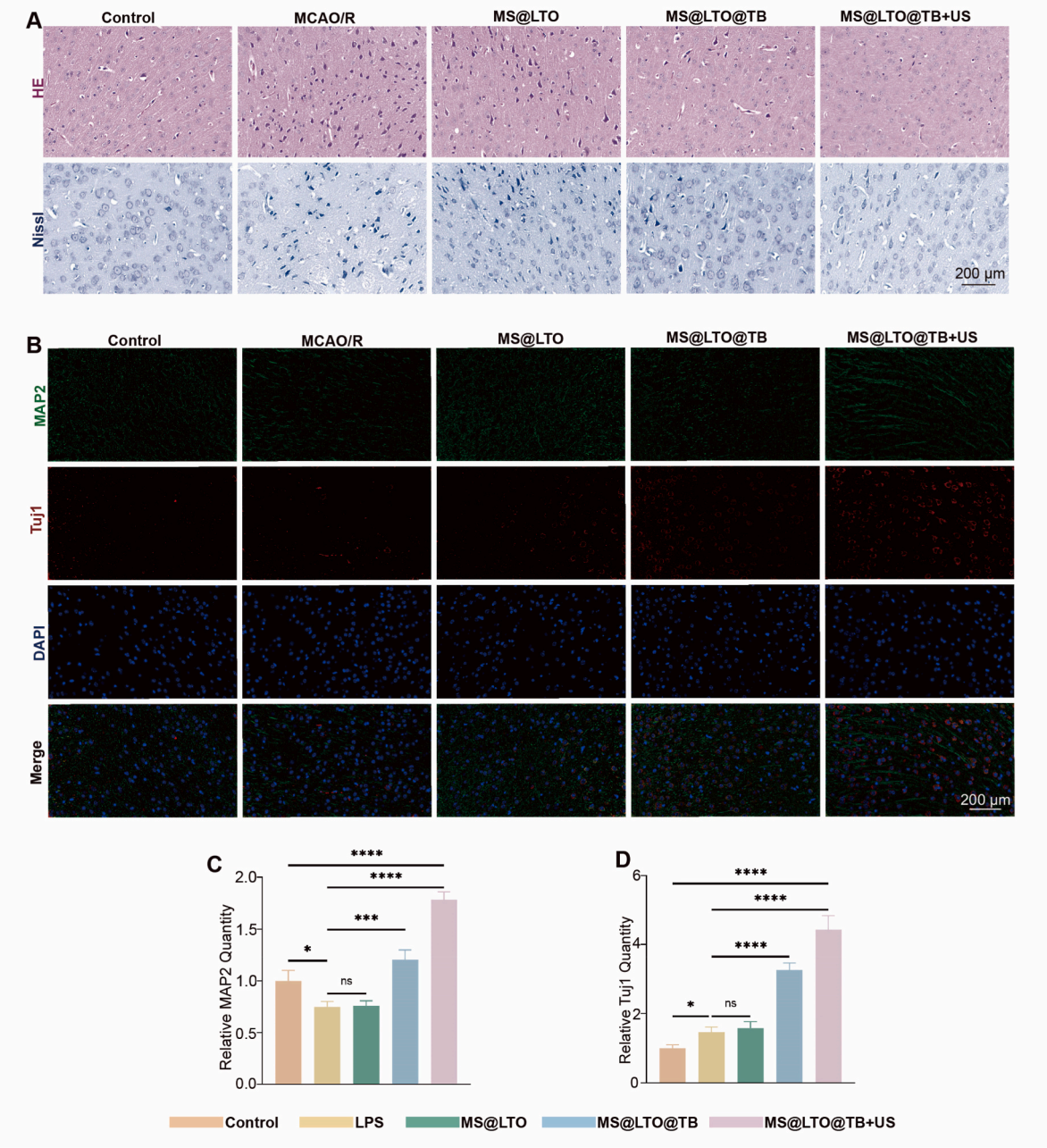

Fig. 8. Neuroprotective and neuroregenerative effects of MS@LTO@TB in vivo. A) H&E and Nissl staining of the brains of MCAO/R model mice sacrificed after different treatments. Scale bar, 200 μm. B) Images of costaining for MAP2 and Tuj1 on the injured side of the brain in different groups. Scale bar, 200 μm. C, D) Statistical analysis of MAP2 and Tuj1 staining according to IF images. n = 5 for each group. The data are presented as mean ± SD (n = 5) for each group. ns: no significance; *P < 0.05, **P < 0.01, ***P < 0.001, ****P < 0.0001.

3.11. Molecular mechanisms by which MS@LTO@TB treats MCAO/R in mice

To elucidate the molecular mechanisms by which MS@LTO@TB treats MCAO/R, whole-genome RNA sequencing of brain tissues was performed 14 days after treatment, and the transcription levels of 34,746 genes were evaluated. There were 916 differentially expressed genes (DEGs) identified in the MCAO/R group compared to the control group, with 718 genes upregulated (represented as red dots) and 198 genes downregulated (represented as blue dots) (Fig. 9A). In the comparison between the MS@LTO@TB + US group and the MCAO/R group, 3659 genes exhibited differential expression, with 737 genes showing an increase and 2922 genes showing a decrease in expression (Fig. 9B). Hierarchical clustering of the gene expression data demonstrated clear differences between both the control and MCAO/R groups, as well as between the MS@LTO@TB + US and MCAO/R groups. These results underscore the significant alterations in gene expression induced by MS@LTO@TB combined with ultrasound treatment.

KEGG pathway enrichment analysis revealed that the MCAO/R group, with 6945 DEGs, was associated with 176 known pathways when compared to the control group. On the other hand, the MS@LTO@TB + US group showed 27,065 DEGs linked to 215 pathways in comparison with the MCAO/R group (Fig. 9C). Further analysis highlighted substantial changes in the expression of genes within the TNF signaling pathway and other relevant pathways in the MCAO/R group, suggesting a pronounced inflammatory reaction in the brain after ischemia-reperfusion (Fig. 9D). Significant changes in calcium signaling and PI3K-AKT pathway activity were detected in the MS@LTO@TB + US

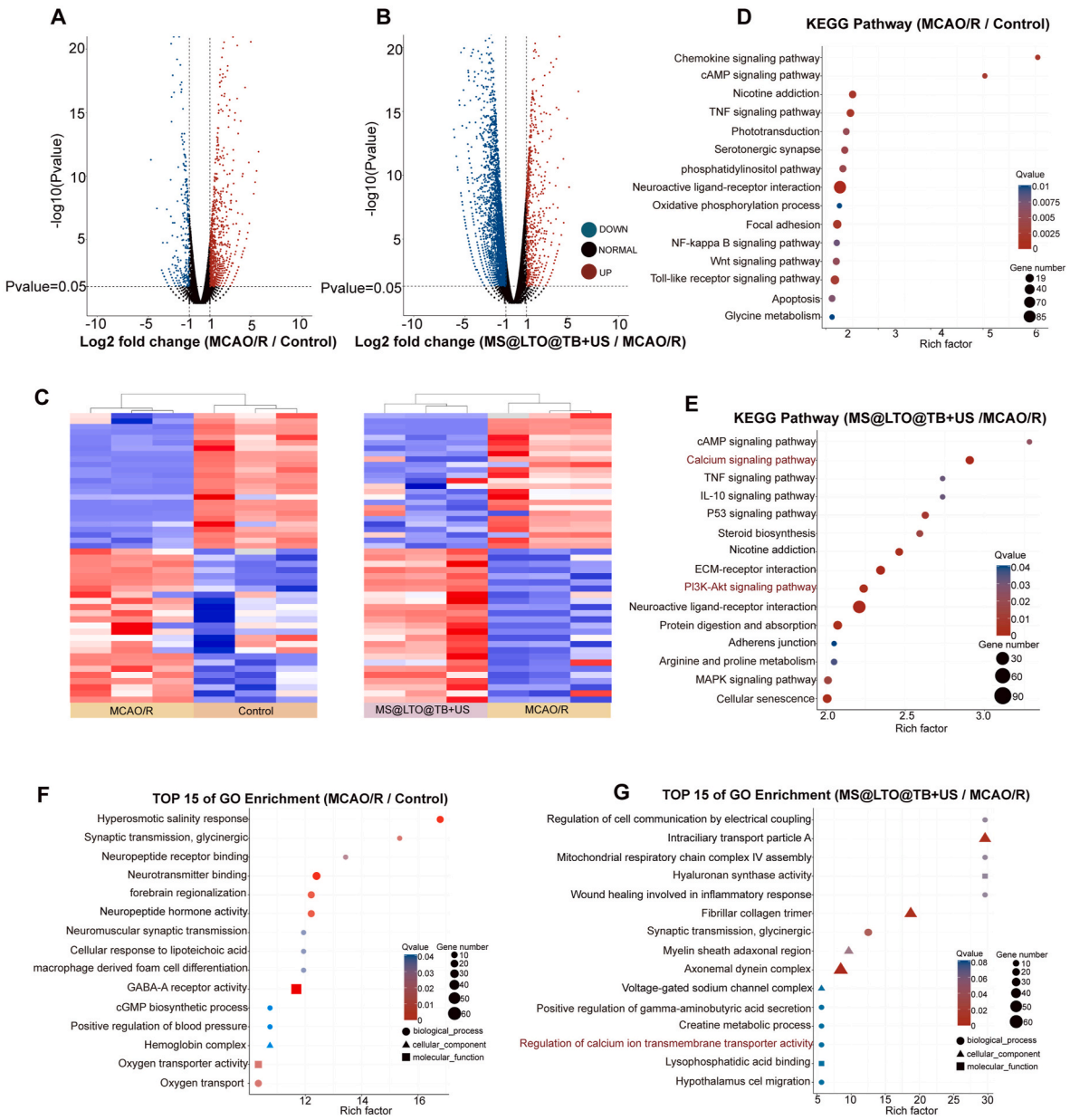

Fig. 9. Evaluation of the effects of MS@LTO@TB on transcriptional profiles in a mouse MCAO/R model. A, B) Volcano plots for the MCAO/R group versus the control group and the MS@LTO@TB + US group versus the MCAO/R group. The upregulated genes are marked in red, and the downregulated genes are marked in blue. C) Heatmap illustrating differential gene expression between the MCAO/R and control groups and between the MS@LTO@TB + US and MCAO/R groups. D, E) KEGG pathway enrichment analysis of the DEGs D) between the MCAO/R group and the control group and E) between the MS@LTO@TB + US group and the MCAO/R group. F, G) Top 15 enriched Gene Ontology (GO) for the DEGs F) between the MCAO/R group and the control group and G) between the MS@LTO@TB + US group and the MCAO/R group.

group compared with the MCAO/R group (Fig. 9E). The PI3K-AKT pathway plays a critical role in neuronal survival and synaptic function. These findings suggest that the piezoelectric effect of MS@LTO@TB under US stimulation effectively mitigates excessive apoptosis and synaptic dysfunction caused by CIRI, which is consistent with the in vitro results.

Further analysis using the Gene Ontology (GO) database identified the molecular functions, cellular components, and biological processes associated with the DEGs. Enrichment analysis revealed significant changes in the expression of genes associated with blood pressure regulation, neuroprotection, oxygen transport, and neurotransmission in the MCAO/R group compared with the control group, suggesting that these processes are key factors in the pathophysiology of IS (Fig. 9F). The pathways in which the DEGs between the MS@LTO@TB + US group and the MCAO/R group were significantly enriched included calcium transmembrane transporter activity, electrical coupling regulation of cell communication, and hypothalamic cell migration. The differential expression of genes enriched in calcium transmembrane transporter activity pathways suggests that the piezoelectric effect of MS@LTO@TB under US treatment significantly increases intracellular calcium activity (Fig. 9G). The differential expression of genes enriched in pathways related to electrical coupling regulation of cell communication and hypothalamic cell migration indicates that US can promote neural cell communication and migration, facilitating neurogenesis and repair.

4. Conclusion

In this study, we developed an ultrasonic nasal drop, MS@LTO@TB,

for noninvasive and efficient repair of CNS damage after thrombolysis for IS. Liposomes loaded with the natural anti-inflammatory drug TB were coated onto BTO to form LTO@TB, which was then encapsulated into aldehyde-modified methacrylic acid HA microspheres to create MS@LTO@TB ultrasonic nasal drops. MS@LTO@TB formed Schiff bases with numerous amino groups in the nasal mucosa, significantly enhancing bioadhesion and transmembrane transport efficiency and resulting in sustained drug release in the brain ventricles. Under US stimulation, the direct piezoelectric effect of LTO@TB electrically stimulated the damaged neurons in a noninvasive manner, promoting the restoration of neuronal electrical conduction. MS@LTO@TB modulated microglial phenotypes, reduced the release of inflammatory mediators, decreased neuronal apoptosis, activated the PI3K/AKT signaling pathway, and promoted the regeneration of damaged axons. In a mouse model of MCAO/R, MS@LTO@TB significantly reduced the infarct volume, alleviated neuroinflammation, and improved cognitive function and memory. This study offers a new perspective for the noninvasive treatment of CNS diseases, demonstrating the significant potential of ultrasonic nasal drops to modulate neuroinflammation and restore neuronal electrical signal conduction.

5. Discussion

This study presents the MS@LTO@TB ultrasonic nasal drop platform, offering significant clinical potential, particularly in neural tissue engineering. Through a non-invasive nasal-to-brain drug delivery route, we overcome the BBB, achieving sustained and efficient drug delivery to the CNS. This approach not only introduces a novel therapeutic framework for IS but also facilitates targeted CNS drug delivery. MS@LTO@TB enhances drug bioavailability through its unique structural advantages and promotes nerve injury repair via a synergistic, multi-mechanistic approach. In the MCAO/R mouse model, it significantly improved neurological recovery post-thrombolysis, especially cognitive function and memory, highlighting its potential for neurodegenerative disease treatment. However, the clinical translation of MS@LTO@TB faces challenges, including ensuring long-term stability, avoiding immune responses during drug release, and minimizing toxicity in practical applications, which need to be addressed in future studies. Based on the current findings and their limitations, future research should focus on the following key areas: First, expanding the scale and variety of animal experiments, particularly validating MS@LTO@TB in non-human primate models, to assess its long-term efficacy and safety across different pathological states. This will not only help elucidate its preclinical efficacy but also provide a solid data foundation for clinical trials. Second, further exploration of this drug delivery system's potential in other central nervous system diseases, particularly in Alzheimer's disease, Parkinson's disease, and other neurodegenerative disorders, should be pursued to validate its efficacy and mechanisms in different pathological contexts. Lastly, a deeper investigation into the molecular mechanisms of MS@LTO@TB, particularly its precise regulatory pathways in neural repair, immune modulation, and anti-inflammatory responses, should be conducted to provide theoretical support for more precise drug design and therapeutic optimization.

In conclusion, this study not only opens up a new therapeutic approach for the treatment of ischemic stroke but also provides a viable solution for non-invasive treatments of central nervous system diseases. MS@LTO@TB demonstrates significant potential in improving neurological function and promoting neural repair, especially within the context of modern nanotechnology and neurobiology, laying a strong foundation for future clinical translation and widespread application. With further optimization and validation, this research has the potential to lead the new era of neurodrug delivery and treatment, bringing breakthrough advancements to clinical medicine.

CRediT authorship contribution statement

Ning Zhu: Writing – original draft, Software, Methodology, Data curation. **Fan Wang:** Software, Methodology, Data curation. **Zeyu Han:** Software, Methodology. **Shifeng Ling:** Software, Investigation. **Duo Wai-Chi Wong:** Visualization, Software. **Shenglin Ye:** Methodology, Investigation, Data curation. **Mingyue Liu:** Visualization, Software, Investigation. **Yanyang Chen:** Methodology, Data curation. **Gracie Shen:** Methodology. **Ming Ni:** Writing – original draft, Visualization, Supervision, Funding acquisition. **Huitong Ruan:** Writing – original draft, Visualization, Validation, Software, Methodology, Investigation, Formal analysis, Data curation, Conceptualization. **Yan Qiu:** Writing – original draft, Supervision, Resources, Project administration, Methodology, Investigation, Funding acquisition. **Wenguo Cui:** Writing – review & editing, Supervision, Methodology.

Ethics approval and consent to participate

All the animal experiments in this study were approved by the Animal Research Committee of Shanghai Pudong New Area People's Hospital (Ethical Approval No. 2022K83). All the authors were in compliance with all relevant ethical regulations.

Declarations of competing interest

The authors declare that they have no known competing financial interests or personal relationships that could have appeared to influence the work reported in this paper.

Acknowledgments

N. Zhu, F. Wang, and Z. Han contributed equally to this work.

This work was funded by: Funded by Outstanding Leaders Training Program of Pudong New Area Health System of Shanghai (Grant No. PWRl 2020–08), Important Weak Subject Construction Project of Pudong Health and Family Planning Commission of Shanghai (Grant No. PWZbr2022-13), National Natural Science Foundation of China (82372120; 82272128), "Chenguang Program" (22CGA16) supported by Shanghai Education Development Foundation and Shanghai Municipal Education Commission, "Two Hundred Talent" Program supported by Shanghai Jiao Tong University School of Medicine (20240701), China Postdoctoral Science Foundation (2023M742360, 2023M742361, and GZB20230443), China National Postdoctoral Program for Innovative Talents (BX20230228).

Appendix A. Supplementary data

Supplementary data to this article can be found online at https://doi.org/10.1016/j.bioactmat.2025.02.022.

References

[1] H. Ruan, Y. Li, C. Wang, Y. Jiang, Y. Han, Y. Li, D. Zheng, J. Ye, G. Chen, G.-y. Yang, L. Deng, M. Guo, X. Zhang, Y. Tang, W. Cui, Click chemistry extracellular vesicle/peptide/chemokine nanocarriers for treating central nervous system injuries, Acta Pharm. Sin. B 13 (5) (2023) 2202–2218.

[2] Z. Yu, C. Liu, C. Wang, G. Zhao, The past and future depicted by neural electrode technology, Innovat. Med. (2024) 100087.

[3] Y. Shen, X. Cao, M. Lu, H. Gu, M. Li, D.A. Posner, Current treatments after spinal cord injury: cell engineering, tissue engineering, and combined therapies, Smart Medicine 1 (1) (2022) e20220017.

[4] T. Xu, L. Gan, W. Chen, D. Zheng, H. Li, S. Deng, D. Qian, T. Gu, Q. Lian, G. Shen, Q. An, W. Li, Z. Zhang, G.-Y. Yang, H. Ruan, W. Cui, Y. Tang, Bridging immune-neurovascular crosstalk via the immunomodulatory microspheres for promoting neural repair, Bioact. Mater. 44 (2025) 558–571.

[5] W. Yu, E. Gong, B. Liu, L. Zhou, C. Che, S. Hu, Z. Zhang, J. Liu, J. Shi, Hydrogel-mediated drug delivery for treating stroke, Chin. Chem. Lett. 34 (9) (2023) 108205.

[6] X. Sun, H. Ruan, Q. Liu, S. Cao, Q. Jing, Y. Xu, L. Xiong, W. Cui, C. Li, Targeted regulation of neuroinflammation via nanobiosignaler for repairing the central nerve system injuries, Nano Res. 16 (2) (2023) 2938–2948.
[7] M. Tian, Z. Ma, G.-Z. Yang, Micro/nanosystems for controllable drug delivery to the brain, Innovation 5 (1) (2024) 100548.
[8] J. Yang, L. Guo, J. Liao, H. Yi, Nano-enhanced nature medicine for ischemic stroke: opportunities and challenges, Biomedical Technology 7 (2024) 32–45.
[9] J. Wang, Q. Wang, Y. Fu, M. Lu, L. Chen, Z. Liu, X. Fu, X. Du, B. Yu, H. Lu, W. Cui, Swimming short fibrous nasal drops achieving intraventricular administration, Science Bulletin 69 (9) (2024) 1249–1262.
[10] U.K. Sukumar, R.J.C. Bose, M. Malhotra, H.A. Babikir, R. Afjei, E. Robinson, Y. Zeng, E. Chang, F. Habte, R. Sinclair, S.S. Gambhir, T.F. Massoud, R. Paulmurugan, Intranasal delivery of targeted polyfunctional gold–iron oxide nanoparticles loaded with therapeutic microRNAs for combined theranostic multimodality imaging and presensitization of glioblastoma to temozolomide, Biomaterials 218 (2019) 119342.
[11] C. Wu, B. Li, Y. Zhang, T. Chen, C. Chen, W. Jiang, Q. Wang, T. Chen, Intranasal delivery of paeoniflorin nanocrystals for brain targeting, Asian J. Pharm. Sci. 15 (3) (2020) 326–335.
[12] S. Ruan, J. Li, H. Ruan, Q. Xia, X. Hou, Z. Wang, T. Guo, C. Zhu, N. Feng, Y. Zhang, Microneedle-mediated nose-to-brain drug delivery for improved Alzheimer's disease treatment, J. Contr. Release 366 (2024) 712–731.
[13] M. Zhang, Q. Liu, H. Meng, H. Duan, X. Liu, J. Wu, F. Gao, S. Wang, R. Tan, J. Yuan, Ischemia-reperfusion injury: molecular mechanisms and therapeutic targets, Signal Transduct. Targeted Ther. 9 (1) (2024) 12.
[14] B. Zhang, W. Luo, Y. Cai, L. Liu, X. Ma, W. Yang, S. Meng, G. Zhao, A. Sun, J. Ge, Global burden of adolescent and young adult cardiovascular diseases and risk factors: results from Global Burden of Disease Study 2019, Innovat. Med. 2 (2) (2024) 100063.
[15] D. Xu, S. Fu, H. Zhang, W. Lu, J. Xie, J. Li, H. Wang, Y. Zhao, R. Chai, Ultrasound-responsive aligned piezoelectric nanofibers derived hydrogel conduits for peripheral nerve regeneration, Adv. Mater. 36 (28) (2024) 2307896.
[16] Y. Chen, G. Wang, F. Zhou, Z. Yin, F. Shen, W. Weng, H. Zhang, Y. Jiang, X. Liu, Y. Deng, Y. Chen, K. Xu, J. Su, Targeting TRPA1 with liposome-encapsulated drugs anchored to microspheres for effective osteoarthritis treatment, Chin. Chem. Lett. (2024) 110053.
[17] Q. Wang, H. Chen, X.Y. Zhou, W. Hailong, H. Wang, J. Zhang, W. Feng, Size-dependent translocation pattern, chemical and biological transformation of nano- and submicron-sized ferric oxide particles in the central nervous system, J. Nanosci. Nanotechnol. 16 (2016) 5553–5561.
[18] A. Mistry, S. Stolnik, L. Illum, Nose-to-Brain delivery: investigation of the transport of nanoparticles with different surface characteristics and sizes in excised porcine olfactory epithelium, Mol. Pharm. 12 (8) (2015) 2755–2766.
[19] Y. Chen, C. Zhang, Y. Huang, Y. Ma, Q. Song, H. Chen, G. Jiang, X. Gao, Intranasal drug delivery: the interaction between nanoparticles and the nose-to-brain pathway, Adv. Drug Deliv. Rev. 207 (2024) 115196.
[20] V. Bourganis, O. Kammona, A. Alexopoulos, C. Kiparissides, Recent advances in carrier mediated nose-to-brain delivery of pharmaceutics, Eur. J. Pharm. Biopharm. 128 (2018) 337–362.
[21] N. Kamei, M. Takeda-Morishita, Brain delivery of insulin boosted by intranasal coadministration with cell-penetrating peptides, J. Contr. Release 197 (2015) 105–110.
[22] W. Chen, D. Zheng, H. Chen, T. Ye, Z. Liu, J. Qi, H. Shen, H. Ruan, W. Cui, L. Deng, Circadian clock regulation via biomaterials for nucleus pulposus, Adv. Mater. 35 (32) (2023) 2301037.
[23] D. Zheng, W. Chen, T. Chen, X. Chen, J. Liang, H. Chen, H. Shen, L. Deng, H. Ruan, W. Cui, Hydrogen ion capturing hydrogel microspheres for reversing inflammaging, Adv. Mater. 36 (5) (2024) 2306105.
[24] X. Han, S. Chen, Z. Cai, Y. Zhu, W. Yi, M. Guan, B. Liao, Y. Zhang, J. Shen, W. Cui, D. Bai, A diagnostic and therapeutic hydrogel to promote vascularization via blood sugar reduction for wound healing, Adv. Funct. Mater. 33 (14) (2023) 2213008.
[25] L. Zhang, L. Pang, S. Zhu, J. Ma, R. Li, Y. Liu, L. Zhu, X. Zhuang, W. Zhi, X. Yu, L. Du, H. Zuo, Y. Jin, Intranasal tetrandrine temperature-sensitive in situ hydrogels for the treatment of microwave-induced brain injury, Int. J. Pharm. 583 (2020) 119384.
[26] L. Racioppi, A.R. Means, Calcium/calmodulin-dependent kinase IV in immune and inflammatory responses: novel routes for an ancient traveller, Trends Immunol. 29 (12) (2008) 600–607.
[27] Y. Xiang, Y. Long, Q. Yang, C. Zheng, M. Cui, Z. Ci, X. Lv, N. Li, R. Zhang, Pharmacokinetics, pharmacodynamics and toxicity of Baicalin liposome on cerebral ischemia reperfusion injury rats via intranasal administration, Brain Res. 1726 (2020) 146503.
[28] G.-M. Dong, H. Yu, L.-B. Pan, S.-R. Ma, H. Xu, Z.-W. Zhang, P. Han, J. Fu, X.-Y. Yang, A. Keranmu, H.-T. Niu, J.-D. Jiang, Y. Wang, Biotransformation of Timosaponin BII into seven characteristic metabolites by the gut microbiota, Molecules 26 (13) (2021) 3861.
[29] X. Zhao, C. Liu, Y. Qi, L. Fang, J. Luo, K. Bi, Y. Jia, Timosaponin B-II ameliorates scopolamine-induced cognition deficits by attenuating acetylcholinesterase activity and brain oxidative damage in mice, Metab. Brain Dis. 31 (6) (2016) 1455–1461.
[30] W.-Q. Lu, Y. Qiu, T.-J. Li, X. Tao, L.-N. Sun, W.-S. Chen, Timosaponin B-II inhibits pro-inflammatory cytokine induction by lipopolysaccharide in BV2 cells, Arch Pharm. Res. (Seoul) 32 (9) (2009) 1301–1308.
[31] T.-J. Li, Y. Qiu, P.-Y. Yang, Y.-C. Rui, W.-S. Chen, Timosaponin B-II improves memory and learning dysfunction induced by cerebral ischemia in rats, Neurosci. Lett. 421 (2) (2007) 147–151.
[32] M. Feng, Y. Zhou, Z. Gao, W. Huang, W. Xie, W. Xie, Z. Liu, S. Tang, X. Xiong, Y. Chen, X. Zhou, C. Liu, Timosaponin BII reduces colonic inflammation and alleviates DSS-induced ulcerative colitis by inhibiting NLRP3, J. Ethnopharmacol. 325 (2024) 117885.
[33] A. Cartier, B. Yeung, J. Moyron-Quiroz, Q. Gao, T.S. Hunag, K. Nazor, M. Tan, Proteomic analysis of microglia during LPS-induced acute neuroinflammation, Alzheimer's Dementia 16 (S4) (2020) e040068.
[34] X. Xiang, X. Xin, Y. Hou, Y. Deng, X. Liu, W. Yu, Diosgenin alters LPS-induced macrophage polarization by activating PPARγ/NF-κB signaling pathway, Int. Immunopharmacol. 126 (2024) 111270.
[35] X. Tian, Z. Peng, S. Luo, S. Zhang, B. Li, C. Zhou, H. Fan, Aesculin protects against DSS-Induced colitis though activating PPARγ and inhibiting NF-κB pathway, Eur. J. Pharmacol. 857 (2019) 172453.
[36] P. Feng, Y.-w. Xu, B. Tong, X.-y. Tong, Y. Bian, S. Zhao, H. Shen, Saikosaponin a attenuates hyperlipidemic pancreatitis in rats via the PPAR-γ/NF-κB signaling pathway, Exp. Ther. Med. 19 (2019) 1203–1212.
[37] K.-Y. Ji, K.M. Kim, Y.H. Kim, A.R. Im, J.Y. Lee, B. Park, M. Na, S. Chae, The enhancing immune response and anti-inflammatory effects of Anemarrhena asphodeloides extract in RAW 264.7 cells, Phytomedicine 59 (2019) 152789.
[38] W. Qin, L. Li, W. Niu, W.R. Wang, D.W. Wu, C.G. Song, C.H. Gao, Z. Mu, F. Tay, K. Jiao, L. Niu, Effects of electric field-modulated conductive hydrogel on osseoperception and osseointegration of dental implants, Adv. Funct. Mater. 34 (2024).
[39] N. Philips, M. Portillo-Esnaola, P. Samuel, M. Gallego-Rentero, T. Keller, J. Franco, Anti-aging and anti-carcinogenic effects of 1α, 25-dihyroxyvitamin D_3 on skin, Plastic and Aesthetic Research 9 (0) (2022) 4.
[40] N.A. Courtney, J.S. Briguglio, M.M. Bradberry, C. Greer, E.R. Chapman, Excitatory and inhibitory neurons utilize different Ca^{2+} sensors and sources to regulate spontaneous release, Neuron 98 (5) (2018) 977–991.e5.
[41] T. Lu, H. Li, Y. Zhou, W. Wei, L. Ding, Z. Zhan, W. Liu, J. Tao, X. Xue, Neuroprotective effects of alisol A 24-acetate on cerebral ischaemia–reperfusion injury are mediated by regulating the PI3K/AKT pathway, J. Neuroinflammation 19 (1) (2022) 37.
[42] W.T. Kimberly, B.G. Dutra, A.M.M. Boers, H.C.B.R. Alves, O.A. Berkhemer, L. van den Berg, K.N. Sheth, Y.B.W.E.M. Roos, A. van der Lugt, L.F.M. Beenen, D.W. J. Dippel, W.H. van Zwam, R.J. van Oostenbrugge, H.F. Lingsma, H. Marquering, C.B.L.M. Majoie, f.t.M.C. Investigators, Association of reperfusion with brain edema in patients with acute ischemic stroke: a secondary analysis of the MR CLEAN trial, JAMA Neurol. 75 (4) (2018) 453–461.